

1 **Four-Dimensional paleomagnetic dataset: Late Neogene**  
2 **paleodirection and paleointensity results from the**  
3 **Erebus Volcanic Province, Antarctica**

4 **H. A. Asefaw<sup>1</sup>, L. Tauxe<sup>1</sup>, A.A.P. Koppers<sup>2</sup>, H. Staudigel<sup>1</sup>**

5 <sup>1</sup>Geosciences Research Division, Scripps Institution of Oceanography, University of California San Diego,  
6 La Jolla, California, USA

7 <sup>2</sup>College of Earth, Ocean and Atmospheric Sciences, Oregon State University, Corvallis, Oregon, USA,

8 **Key Points:**

- 9
- 10 • We present 11 new  $^{40}\text{Ar}/^{39}\text{Ar}$  age determinations from the Erebus Volcanic Province,  
Antarctica ( $-78^\circ$ ,  $167^\circ$ ).
- 11 • We present 107 high quality site directions resulting in VGP scatter consistent with  
model predictions and a paleopole consistent with GAD.
- 12 • We present 28 new paleointensities that yield an estimated average dipole moment  
of  $43 \pm 3.4 \text{ ZAm}^2$ .
- 13
- 14

15 **Plain Language Summary**

16 The GAD hypothesis states that the Earth's magnetic field may be approximated  
17 by an Earth-centric dipole aligned with the rotation axis. This hypothesis is fundamen-  
18 tal for paleogeographic reconstructions of the tectonic plates. While global paleomag-  
19 netic directions from the last 10 Myrs recover a predominately GAD field structure, pa-  
20 leointensity estimates over the same time period do not. In this study, we re-examine  
21 the paleomagnetic field structure in the Erebus Volcanic Province, Antarctica, and re-  
22 cover a robust dataset of directional and intensity data. We then compare the paleopole  
23 and average dipole moment against a GAD field structure and model predictions of pa-  
leosecular variation.

24

---

Corresponding author: Hanna Asefaw, [hasafaw@ucsd.edu](mailto:hasafaw@ucsd.edu)

25 **Abstract**

26 A fundamental assumption in paleomagnetism is that a geocentric axial dipole (GAD)  
 27 geomagnetic field structure extends to the ancient field. Global paleodirectional com-  
 28 pilations that span 0 - 10 Myr support a GAD dominated field structure with minor non-  
 29 GAD contributions, however, the paleointensity data over the same period do not. In  
 30 a GAD field, higher latitudes should preserve higher intensity, but the current database  
 31 suggests that intensities are independent of latitude. To determine whether the seem-  
 32 ingly “low” intensities from Antarctica reflect the ancient field, rather than low quality  
 33 data or inadequate temporal sampling, we have conducted a new study of the paleomag-  
 34 netic field in Antarctica. This study focuses on the paleomagnetic field structure over  
 35 the Late Neogene. We combine and re-analyze new and published paleodirectional and  
 36 paleointensity results from the Erebus volcanic province to recover directions from 107  
 37 sites that were both thermally and AF demagnetized and then subjected to a set of strict  
 38 selection criteria and 28 paleointensity estimates from specimens that underwent the IZZI  
 39 modified Thellier-Thellier experiment and were also subjected to a strict set of selection  
 40 criteria. The paleopole ( $205.6^\circ$ ,  $87.1^\circ$ ) and  $\alpha_{95}$  ( $5.5^\circ$ ) recovered from our paleodirectional  
 41 study supports the GAD hypothesis and the scatter of the virtual geomagnetic poles is  
 42 within the uncertainty of that predicted by TK03 paleosecular variation model. Our time  
 43 averaged field strength estimate,  $33.01 \mu\text{T} \pm 2.59 \mu\text{T}$ , is significantly lower than that ex-  
 44 pected for a GAD field estimated from the present field, but consistent with the long term  
 45 average field.

46 **1 Introduction**

47 A geocentric axial dipole (GAD) field is the magnetic field generated by a dipole  
 48 that is positioned in the center of the Earth and aligned along the spin axis (Gilbert, 1958).  
 49 In mathematical representations of the geomagnetic field structure, such as the Inter-  
 50 national Geomagnetic Reference Field (IGRF), the axial dipole term ( $g_1^0$ ) accounts for  
 51 the majority of the field (Lowes, 1973). However, modern geomagnetic field strengths  
 52 around the globe (Figure 1a) reveal latitudinal and longitudinal non-GAD features and  
 53 regions with anomalously low (e.g. the South Atlantic Anomaly, or SAA) and high (e.g.  
 54 south of Australia) intensities. It is frequently assumed (e.g., (McElhinny, 2007) that  
 55 the field, when averaged over sufficient time, is well approximated by a GAD field. Given  
 56 a GAD field (Figure 1b) both the intensity of the geomagnetic field ( $B$ ) and the incli-  
 57 nation ( $I$ ) would vary with latitude ( $\lambda$ ) by:

$$B = M \sqrt{1 + 3 \cos^2(\frac{\pi}{2} - \lambda)} \quad (1)$$

58 and

$$\tan(I) = 2 \tan(\lambda) \quad (2)$$

59 where  $M$  is the  $g_1^0$  term in nT (and also the intensity of the field at the equator).

60 Both the GAD and non-GAD terms of the geomagnetic field vary with time, a phe-  
 61 nomenon known as secular variation. The terms of the IGRF have been estimated for  
 62 the last century or so (Thébault et al., 2015), using geomagnetic observatory and, more  
 63 recently, satellite data. From 1600 to modern geomagnetic observatories, IGRF-like mod-  
 64 els were based on ship-board measurement data (Jackson et al., 2000). Prior to about  
 65 1600, measurements of the geomagnetic field are too scarce for constraining reference mod-  
 66 els and so we rely on geologic and archaeologic materials (e.g., Constable et al. (2016)  
 67 and references therein). The paleomagnetic field structure can be preserved in the ge-

68 ological record and various techniques allow us to recover paleodirections (Irving et  
 69 al., 1961; Creer, 1967; Stephenson, 1967) and paleointensities (Thellier & Thellier, 1959;  
 70 Shaw, 1974; Coe, 1967; Yu et al., 2004; Walton & Shaw, 1922; Hoffman & Biggin, 2005).  
 71 Independent studies of the paleofield are then compiled into paleomagnetic databases  
 72 (e.g., the MagIC database at: [earthref.org/MagIC](https://earthref.org/MagIC)). We can then use these data to char-  
 73 acterize the behavior of paleosecular variation (PSV) and the time averaged field (TAF).  
 74 Changes in the structure of the geomagnetic field at the surface of the Earth reflect the  
 75 dynamics occurring in the fluid outer core (Glatzmaier & Coe, 2007; Jackson & Finlay,  
 76 2007; Holme, 2007; Livermore et al., 2014) so an accurate characterization of the field  
 77 is important for understanding the outer core.

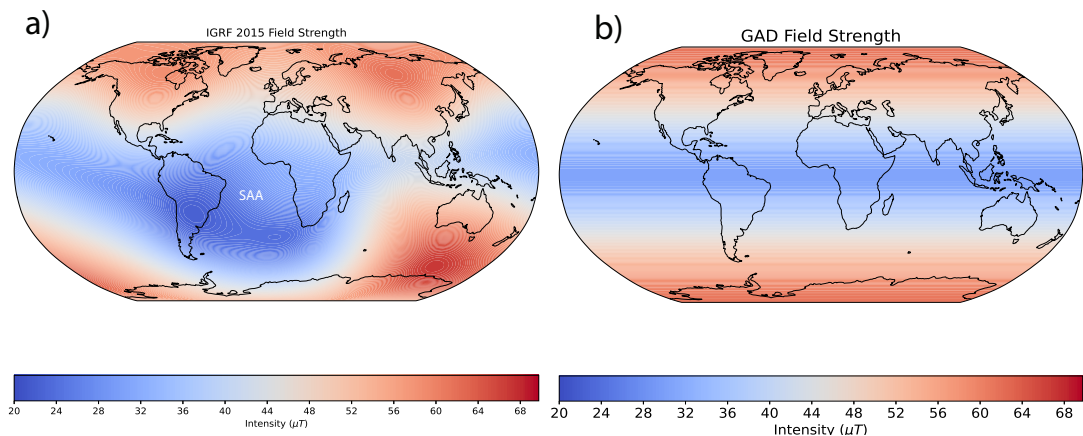


**Figure 1.** a) Intensity of the geomagnetic field estimated from the 2015 IGRF model. b) Intensity of the geomagnetic field expected for a GAD field with an  $80 \text{ ZAm}^2$  magnetic moment.

78 Numerous studies (Opdyke & Henry, 1969; McElhinny & Lock, 1996; Johnson et  
 79 al., 2008; Cromwell, Tauxe, et al., 2018; Behar et al., 2019) have recovered paleodirec-  
 80 tions from the Neogene that are largely consistent with a GAD field with small non-GAD  
 81 terms. Early compilations of absolute paleointensities were also interpreted as largely  
 82 consistent with a GAD structure (McFadden & McElhinny, 1982; Tanaka et al., 1995)  
 83 with a paleomagnetic dipole moment (PDM) similar to the present dipole moment of  $\sim 80$   
 84  $\text{ZAm}^2$ . When considering data from submarine basaltic glass over the last five million  
 85 years, Selkin and Tauxe (2000) found a reasonable fit to intensities predicted by a PDM  
 86 of  $\sim 45 \text{ ZAm}^2$ . However, the dipole signature is not evident in modern absolute paleoin-  
 87 tensity databases, which include data from a variety of materials and methods (e.g., PINT15  
 88 of Biggin (2010) and the MagIC database at <https://earthref.org/MagIC>) over the same  
 89 time period (Lawrence et al., 2009; Tauxe & Yamazaki, 2015; Wang et al., 2015), see Fig-  
 90 ure 2). The lack of a dipole signal in the current global database may reflect a paleomag-  
 91 netic field structure with stronger non-GAD components than previously recognized or  
 92 a bias in the global data set as a consequence of poor temporal sampling, poor exper-  
 93 imental design or poor choice of sample materials. Therefore, the reliability of the data  
 94 from high southerly latitudes is key to understanding the behavior of the geomagnetic  
 95 field.

96 Recovering paleointensity is challenging owing to the complex magnetization ac-  
 97 quisition behavior of non-ideal magnetic grains (Dunlop et al., 2005; Dunlop & Özdemir,  
 98 2001; Tauxe & Yamazaki, 2015) and the tendency for magnetomineralogical alteration  
 99 during paleointensity experiments (Coe, 1967; Smirnov & Tarduno, 2003). To determine  
 100 whether the ‘low’ intensities measured at the high southerly latitudes are an artifact of  
 101 non-ideal magnetic recorders or are in fact an accurate representation of the paleomag-  
 102 netic field structure, we conducted an extensive study of the paleomagnetic field in the  
 103 Erebus Volcanic Province, Antarctica ( $-78^\circ$ ,  $167^\circ$ ). Our goal was to target the finest grained  
 104 (glassiest) material (Selkin & Tauxe, 2000; Cromwell et al., 2015), treat them to a rig-

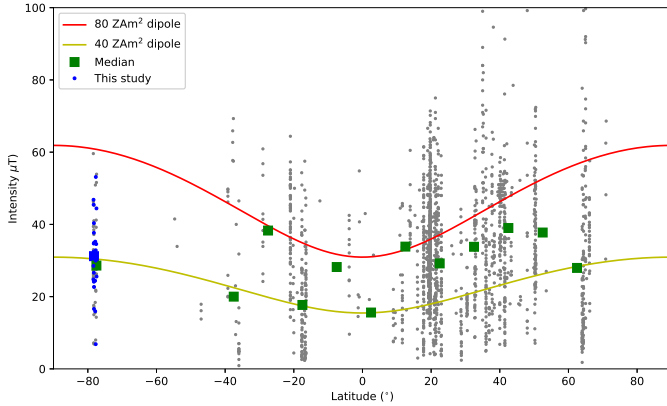


**Figure 2.** Global paleointensity estimates over the last 5 Myr taken from the PINT15 database (Biggin, 2010) of absolute paleointensities (grey circles). The intensity estimates are binned into  $10^{\circ}$  latitude intervals. The median value of bins with 10 or more sites is plotted as green squares. The results from this study are marked as blue points along with their median intensity (blue square). The yellow curve (red curve) marks the intensity at a given latitude expected for a dipole moment of  $40 \text{ ZAm}^2$  ( $80 \text{ ZAm}^2$ ).

105 orous experimental protocol (Yu et al., 2004) and subject the results to a set of strict  
106 selection criteria (Cromwell et al., 2015).

## 107 2 Methods

### 108 2.1 Sample Collection

109 Mankinen and Cox (1988) drilled between 6 and 8 oriented core samples from the  
110 interior of lava flows around the Erebus Volcanic Province, Antarctica (Figure 3) and  
111 reported directions from the natural remanent magnetization (NRM). Tauxe et al. (2004)  
112 analyzed the Mankinen/Cox sample collection for directions and intensities. Lawrence  
113 et al. (2009) reported on a larger suite of samples collected in two field seasons (2003/2004  
114 and 2005/2006), which included at least 10 cores per lava flow; they compiled all the pa-  
115 leodirectional and paleointensity experiments from these cores and those collected ear-  
116 lier by Mankinen and Cox (1988).

117 Several recent studies (e.g., Cromwell et al. (2015)) have suggested that finer grained  
118 lava flow tops, as opposed to flow interiors, coupled with the use of stricter selection cri-  
119 teria, may result in more accurate and precise estimates of paleointensity. We therefore  
120 applied the selection criteria proposed by Cromwell et al. (2015) to reanalyze the pale-  
121 ointensity results of Lawrence et al. (2009). In our reanalysis, only a dozen of the orig-  
122 inal 41 sites pass the CCRIT criteria. Therefore, in the 2015/2016 field season, we re-  
123 sampled nearly all of the original sites reported by Lawrence et al. (2009) (141 total) for  
124 this study, targeting only the surfaces of each lava flow. Where possible, we identified  
125 the original sites (Table 3) using the 1-inch drill holes remaining in the outcrop. The re-  
126 mainder were located by GPS coordinates from Lawrence et al. (2009) and approximated  
127 from the maps and descriptions in Mankinen and Cox (1988). Once we identified the orig-  
128 inal sampling sites, we re-sampled the microcrystalline, glassy material from the lava flow  
129 top or flow bottom. We collected hand samples using hammers and chisels. The outcrops  
130 included lava flows, pillow lavas, and hyaloclastite cones that formed over the Late Neo-

131 gene. Several sites from the original study recover identical paleodirections and re-examination  
 132 in the field confirmed that these sites sampled the same lava flow, so in this study, we  
 133 combine these replicates into single sites (see supporting information Table S1).

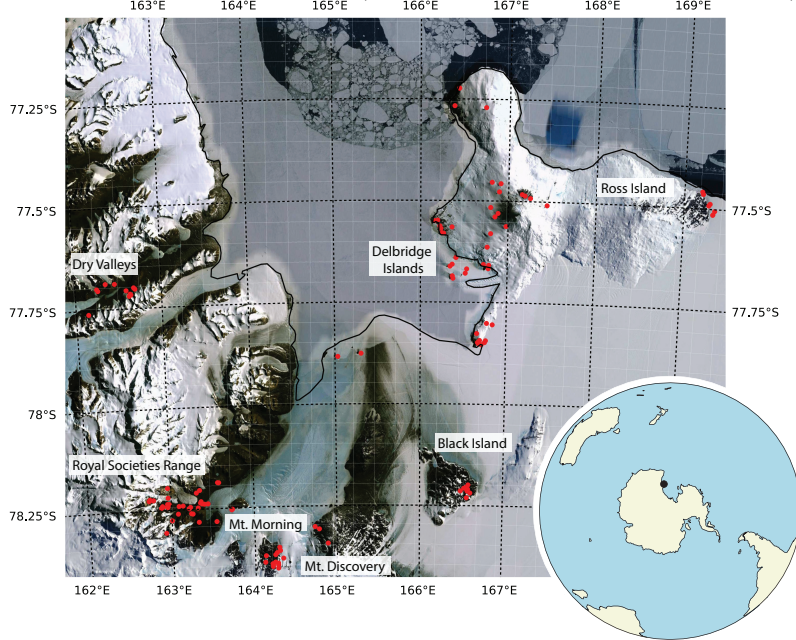


**Figure 3.** A natural color satellite image of the Erebus Volcanic Province, Antarctica. Our sites (red circles) include the Dry Valleys, Royal Societies Range, Mt. Morning, Mt. Discovery, Black Island, and Ross Island.

## 134 2.2 Paleointensity

### 135 2.2.1 Recovering paleointensity

136 Magnetic grains in igneous rocks acquire a thermal remanent magnetization (TRM)  
 137 by cooling from temperatures well above their Curie temperature through their block-  
 138 ing temperatures ( $T_b$ ). Once the grain cools below  $T_b$ , the resulting TRM captures an  
 139 instantaneous record of the geomagnetic field that can remain stable over long timescales.  
 140 The degree of alignment between the magnetic grain moments and the ambient field de-  
 141 pends on the strength of the field ( $B$ ) at the time of cooling (Néel, 1955). For a given  
 142 population of magnetic grains,

$$M_{TRM} = M_s \tanh \frac{v M_s(T_b) B}{k T_b}, \quad (3)$$

143 where  $M_{TRM}$  is the net magnetization,  $k$  is the Boltzmann constant,  $v$  is magnetic grain  
 144 volume, and  $M_s(T_b)$  is spontaneous magnetization at  $T_b$ .

145 In a weak magnetic field (of the order of the modern geomagnetic field), TRM ac-  
 146 quisition is generally assumed to be quasi-linearly proportional to the strength of the am-  
 147 bient field. This proportionality allows us to recover the intensity of the geomagnetic field  
 148 when the rock formed. The NRM may be removed by heating the rock and cooling it  
 149 in zero external field. A new thermal remanent magnetization (TRM) overwrites the NRM  
 150 by cooling the rock in a controlled field in the laboratory. The ratio of the TRM acquired  
 151 in the applied field is proportional to the ratio of the NRM acquired in the paleomag-  
 152 netic field (Néel, 1955). We thus can estimate the intensity of the paleomagnetic field  
 153 by

$$B_{anc} = \frac{M_{NRM}}{M_{TRM}} B_{lab}, \quad (4)$$

where  $M_{NRM}$  is the natural remanent magnetization,  $B_{lab}$  is the field applied in the lab,  $M_{TRM}$  is the thermal remanent magnetization imparted by heating the specimen, then cooling it in the lab field, and  $B_{anc}$  is the strength of the paleomagnetic field. A rock contains an assemblage of magnetic grains and each grain blocks its magnetization at a different temperature. Therefore incrementally demagnetizing and remagnetizing a rock sample at progressively higher temperatures results in several independent estimates of the paleofield, assuming independence of partial TRMs (pTRM) acquired and lost in different temperature intervals.

### 2.2.2 Specimen preparation

Samples were crushed into 100 – 500 mg fragments. The fragments were then examined under a binocular microscope to select the individual specimens that appeared the freshest and finest grained. These glassy (or microcyrstalline) specimens may contain the single domain grains of magnetite that follow Thellier's laws (Thellier, 1938) and allow us to recover an accurate paleointensity estimate. Each individual specimen was swaddled in glass microfiber filter paper and affixed inside a borosilicate glass vial with  $K_2SiO_3$ . The specimens were then placed in a transformer steel shielded room in the Paleomagnetic Laboratory at Scripps Institution of Oceanography for the duration of the experiment.

### 2.2.3 IZZI modified Thellier-Thellier Experiment

We conducted the IZZI-modified Thellier-Thellier protocol (Yu et al., 2004; Tauxe & Staudigel, 2004), whereby specimens are incrementally heated and cooled either in the absence of a magnetic field to demagnetize the NRM (a zero-field step) or in the presence of an applied lab field to impart a pTRM (an in-field step). Specimens were subjected to both an in-field (I) and zero-field (Z) treatment at each temperature step. Temperature steps were conducted at 100°C intervals from 0°C to 400°C, then 25°C intervals to 500°C, and finally at 10°C intervals until each specimen was completely demagnetized. Specimens were heated in custom-built furnaces in the Scripps Paleomagnetic Laboratory; these furnaces have thermocouples in non-inductively wound heating elements to control the temperature to within a few degrees with reproducibility of better than one degree. Specimens were rapidly air-cooled following treatment. During in-field treatment steps, specimens were cooled in fields of various strengths (initially 30  $\mu$ T). The order of the treatment, IZ (Aitken et al., 1988) or ZI (Coe, 1967), alternated with each temperature step in order to detect tails (pTRMs imparted at a given temperature that were not removed by treatment in zero field at the same temperature), and zero-field memory effects (Aitken et al., 1988) in the ZI sequence. We applied pTRM checks, additional in-field treatments at a previously measured temperature step, between the ZI and the IZ sequences in order to monitor mineral neoformation and magnetomineral alteration (Coe, 1967). Immediately following treatment, we measured the magnetic remanence with a 2G Cryogenic SQUID (superconducting quantum interference device) magnetometer in the Scripps Paleomagnetic Laboratory.

We conducted a preliminary IZZI-modified Thellier Thellier experiment (Yu et al., 2004; Tauxe & Staudigel, 2004) on 144 specimens from 99 samples, with, one to two specimens from each sample. The results from this preliminary experiment allowed us to target our efforts to the most promising sites from which we selected up to six additional specimens. In total, we measured 381 specimens.

199            **2.2.4 Cooling Rate**

200            The TRM acquired by each specimen is affected by its rate of cooling (Dodson &  
 201 McClelland-Brown, 1980; Halgedahl & Fuller, 1980; Fox & Aitken, 1980; Santos & Tauxe,  
 202 2019). After each treatment, specimens were rapidly air-cooled to match the rate at which  
 203 we suspect these very fine grained specimens initially cooled. To assess the possible im-  
 204 pact of cooling rate on TRM acquisition in our specimens compared to those studied by  
 205 (Lawrence et al., 2009) from the presumably slower cooled lava flow interiors, we con-  
 206 ducted a cooling rate experiment whereby we heated the specimens to 620° in a 50  $\mu\text{T}$   
 207 field, cooled them as before (in under an hour), and then measured their TRM. We then  
 208 re-heated the specimens to 620° in a 50  $\mu\text{T}$  field and allowed them to cool without a fan  
 209 (approximately 12 hours), and remeasured the resulting TRM. The ratio of the two mea-  
 210 surements allows us to assess the effect of cooling rate on the TRM.

211            **2.2.5 Non-linear TRM Acquisition**

212            The Thellier method (Thellier & Thellier, 1959) is based on the assumption of sin-  
 213 gle domain (SD) non-interacting grains of magnetite that acquire a TRM in proportion  
 214 to the ambient field in low magnetic fields, yet several studies have detected non-linear  
 215 TRM acquisition (e.g., Selkin et al. (2007); Ben-Yosef et al. (2009)). Therefore after we  
 216 completed the IZZI-experiment, we selected specimens from sites that met the CCRIT  
 217 criteria in both our and Lawrence et al. (2009)'s experiments. For these, we performed  
 218 an additional set of steps to detect non-linear TRM acquisition behavior. We subjected  
 219 these specimens to a total TRM by cooling from 630° C, in treatment fields of 0, 15, 20,  
 220 30, 40, 50, and 60  $\mu\text{T}$ .

221            **2.3 Paleodirection**

222            **2.3.1 Alternating field demagnetization and thermal demagnetization**

223            Lawrence et al. (2009) recovered paleodirections by stepwise thermal demagneti-  
 224 zation or alternating field (AF) demagnetization. Each oriented drill core was cut into  
 225 one-inch specimens, at least five of which were subjected to either AF or thermal demag-  
 226 netization. A total of 461 specimens were AF demagnetized in a Sapphire Instruments  
 227 SI-4 uniaxial AF demagnetizer in the Scripps laboratory. Specimens were treated in 5  
 228 mT steps from 5 mT – 20 mT, 10 mT steps from 20 mT – 100 mT, and then at 120 mT,  
 229 150 mT, and 180 mT or until the NRM was removed. An additional 323 specimens were  
 230 thermally demagnetized by stepwise heating in 50°C intervals from 0°C – 500°C, in 25°C  
 231 intervals from 520°C to 560°C and in 5°C-10°C intervals until the specimens were en-  
 232 tirely demagnetized. After each treatment, the remaining NRM was measured. The de-  
 233 magnetization path, as represented by Zijderveld diagrams (Zijderveld, 1967) monitors  
 234 the stability and behavior of the magnetization vector as the specimen is demagnetized.  
 235 For this study, we thermally demagnetized an additional 44 specimens to increase the  
 236 number of paleodirectional estimates per site from 5 to 6 following the suggestion of Behar  
 237 et al. (2019) who found decreased scatter and increased consistency with GAD by us-  
 238 ing more specimens per site and stricter within site scatter criteria.

239            **2.4 Hysteresis and FORCs**

240            Lawrence et al. (2009) describe paleointensity experiments on specimens that were  
 241 drilled from the interior of the lava flows including those collected by Mankinen and Cox  
 242 (1988) and analyzed by Tauxe et al. (2004). Here we report on new experiments on sam-  
 243 ples that were hand collected from the surface or base of the lava flow. As described in  
 244 the following, six sites had specimens with successful intensity estimates from samples  
 245 collected from both the interior (presumably coarser grained) and the flow top. We se-  
 246 lected sister specimens from these sites and measured hysteresis loops and FORC dia-

grams (Roberts & Verosub, 2000) with a Princeton Measurements Corporation Micro-mag Alternating Gradient Magnetometer in an attempt to diagnose domain state. We plotted the results using the FORCinel software package (Harrison & Feinberg, 2008).

## 250 2.5 $^{40}\text{Ar}/^{39}\text{Ar}$ Geochronology

251 Eighteen samples were selected for  $^{40}\text{Ar}/^{39}\text{Ar}$  age dating. All Ar-Ar age analyses  
 252 were conducted at the Argon Geochronology lab at Oregon State University following  
 253 the procedure of Koppers et al. (2000); Koppers (2003); Koppers et al. (2008). A 200–300  
 254  $\mu\text{m}$  groundmass specimen was selected from each sample and then rinsed with distilled  
 255 water and leached in an ultrasonic bath with  $\text{HNO}_3^-$  to remove any alteration products.  
 256 Once cleaned, samples were irradiated in the TRIGA CLICIT nuclear reactor at OSU  
 257 to convert  $^{39}\text{K}$  to  $^{39}\text{Ar}$ . The irradiated samples were then incrementally heated in 21–  
 258 44 temperature steps for 5–7 minutes each. At each temperature step, a defocused  $\text{CO}_2$   
 259 laser beam scanned the sample to release the Argon. Argon isotopes were then measured  
 260 by an ARGUS-VI Mass Spectrometer.

261 At each temperature step, Ar isotopes  $^{36}\text{Ar}$ ,  $^{39}\text{Ar}$ , and  $^{40}\text{Ar}$  are measured. The age  
 262 of the sample is estimated by a heating plateau age and an inverse isochron age that are  
 263 compared to ensure the two estimates are concordant at the 95% confidence level. To  
 264 estimate the heating plateau age, an age and uncertainty is first calculated for each tem-  
 265 perature step by using the ratio of  $^{40}\text{Ar}$  to  $^{39}\text{Ar}$ . A plateau is then selected from this age  
 266 spectrum that includes at least three incremental heating steps with overlapping  $2\sigma$  con-  
 267 fidence levels and at least 50% of the total  $^{39}\text{Ar}_k$  released. The heating plateau age of  
 268 the sample is estimated from the mean plateau age and its reliability by the Mean Square  
 269 Weighted Deviate (MSWD). To determine the inverse isochron age, the ratio of  $^{36}\text{Ar}/^{40}\text{Ar}$   
 270 is plotted against  $^{39}\text{Ar}/^{40}\text{Ar}$ . A regression line is selected that includes at least 5 heat-  
 271 ing steps and each data point to within  $3\sigma$  of the  $^{39}\text{Ar}/^{40}\text{Ar}$  and  $^{36}\text{Ar}/^{40}\text{Ar}$  weighted means  
 272 (Heaton & Koppers, 2019). The inverse isochron age is calculated with the value of  $^{39}\text{Ar}/^{40}\text{Ar}$   
 273 when  $^{36}\text{Ar}/^{40}\text{Ar}$  is 0.

## 274 3 Results

### 275 3.1 Paleointensity

276 We present the results of our IZZI experiment as Arai diagrams (Nagata et al., 1963),  
 277 in order to compare the ratio between NRM remaining to pTRM acquired for each pair  
 278 of temperature steps and to monitor any changes in this ratio. We present the magne-  
 279 tization directions as Zijderveld diagrams (Zijderveld, 1967) and calculate the best fit-  
 280 ting direction or plane, through the vectors using principal component analysis (Kirschvink,  
 281 1980). Despite our best effort to collect micro-crystalline material, our specimens often  
 282 did not behave as the non-interacting uniaxial single domain grains of magnetite assumed  
 283 by Néel theory (Néel, 1955) and required by Thellier's Laws (Thellier & Thellier, 1959).  
 284 Instead, many specimens exhibit non-ideal behavior (i.e. zig-zagging, failed pTRM checks,  
 285 or multiple components of magnetization) resulting in potentially unreliable paleointen-  
 286 sity estimates.

#### 287 3.1.1 Non-ideal behavior: Zig-zagging

288 Zig-zagging in the Arai diagram (Figure 4a,e) occurs when the ratio of NRM re-  
 289 maining to pTRM acquired varies between different temperature intervals based on the  
 290 sequence of treatment steps (IZ or ZI). During the IZZI modified Thellier-Thellier ex-  
 291 periment, the order in which the treatments are applied, in-field then zero-field or zero-  
 292 field then in-field, alternates at each temperature step (Yu et al., 2004). The alternating  
 293 sequence is used to detect so-called 'pTRM tails' (Shashkanov & Metallova, 1972)  
 294 and zero-field memory effects (Aitken et al., 1988). Tails occur either when the pTRM

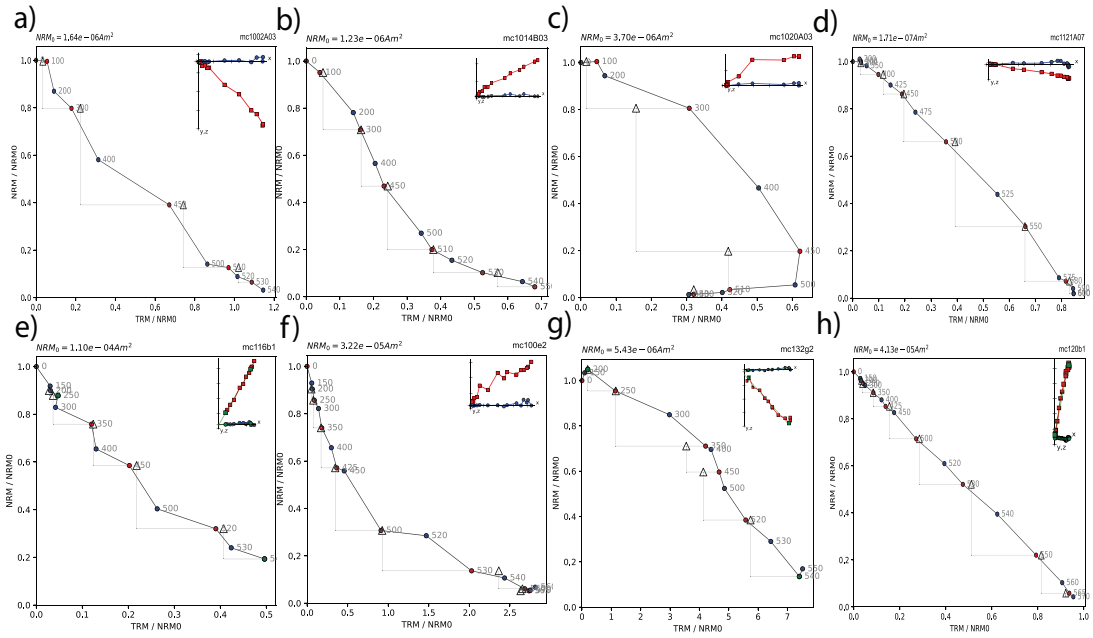


**Figure 4.** Representative Arai and Zijderveld diagrams (insets) of the different behaviors observed in our unoriented specimens. White triangles mark pTRM checks while circles indicate the sequence of treatments- in-field treatment preceding a zero-field treatment (red circles) or zero-field treatment preceding an in-field treatment (blue circles). a - d) are results from this study and e - f) from (Lawrence et al., 2009). a,e) zig-zagging; b,f) non-linearity and sagging; c,g) failed pTRM checks; d,h) ‘well-behaved’ specimens where the proportion of NRM remaining to pTRM acquired is identical between each set of temperature steps.

acquired by heating to temperature  $T$  in a field is not entirely removed when the specimen is reheated to temperature  $T$  and cooled in a zero-field (a high temperature tail) or when the pTRM is removed at a lower temperature (a low temperature tail). This behavior likely indicates the presence of non-SD grains (Dunlop & Özdemir, 2001).

### 3.1.2 Non-ideal behavior: Failed pTRM checks

A pTRM check, for which a previously measured in-field treatment is repeated, is inserted after every ZI-I<sub>Z</sub> pair (Coe, 1967; Tauxe & Staudigel, 2004). Any deviation in the remanence (Figure 4b) indicates magneto-mineral alteration or changes in the blocking and unblocking temperature spectra perhaps due to the presence of non-SD grains (Shcherbakov et al., 1993).

### 3.1.3 Ideal behavior and Selection Criteria

To filter out the specimens that exhibited non-ideal behavior (Figure 4), we applied a set of selection criteria at the specimen and site level. A wide range of selection criteria (Selkin & Tauxe, 2000; Leonhardt et al., 2004; Kissel & Laj, 2004; Tauxe et al., 2016) and paleointensity statistics (Paterson et al., 2014) exists to separate low and high quality paleointensity data. We modeled our criteria (Table 1) after those of Cromwell et al. (2015), in which they successfully recovered accurate and precise estimates of paleointensity of historical Hawaiian lava flows. This set is referred to as the ‘CCRIT’ set of paleointensity criteria (Tauxe et al., 2016).

n	DANG	MAD	$\beta$	SCAT	Frac	$G_{max}$	$ \vec{k} $	N	B%	B $\sigma$
4	$\leq 5^\circ$	$\leq 5^\circ$	0.1	TRUE	0.78	$\leq 0.6$	0.164	3	10	$4 \mu\text{T}$

**Table 1.** Selection criteria (Paterson et al., 2014) applied to the data from the IZZI-modified Thellier-Thellier experiment: n = minimum number of consecutive demagnetization steps, DANG = deviation angle, MAD = maximum angle of deviation,  $\beta$  = the maximum ratio of the standard error to the best fit slope, SCAT = a boolean value that indicates whether the data fall within  $2\sigma_{threshold}$  of the best fit slope, FRAC = fractional remanence,  $G_{max}$  = maximum fractional remanence removed between consecutive temperature steps,  $|\vec{k}|$  = maximum curvature statistic (1/radius of the best-fitting circle), N = minimum number of specimens per sample, B% = maximum percentage standard deviation from the site average intensity,  $B_\sigma$  = maximum intensity ( $\mu\text{T}$ ) deviation from the site average intensity.

CCRIT applies two directional statistics, Deviation ANGle ( $\alpha$  of Selkin and Tauxe (2000),  $dev$  of Tanaka and Kobayashi (2003) and DANG in (Paterson et al., 2014)) and maximum angle of deviation (MAD) (Kirschvink, 1980) to determine the variability in the direction of the NRM. MAD quantifies the amount of scatter in the directions while DANG calculates the angle between the best-fit line for the demagnetization direction and the origin. Three additional parameters are SCAT and FRAC of Shaar and Tauxe (2013), and  $|\vec{k}|$  of Paterson (2011) applied over interval used ( $k'$ ) of (Cromwell et al., 2015); these are applied to test the assumption of linearity of the Arai plot. SCAT constrains the amount of scatter permitted between the best fit proportionality constant and the demagnetization data and pTRM checks; FRAC ensures the majority of the remanence is used to calculate paleointensity;  $|\vec{k}|$  quantifies the amount of curvature. CCRIT also tests for consistency between estimates at the site level by setting thresholds on the percent error ( $\beta_\sigma\%$ ) and standard deviation ( $\beta_\sigma$ ) permitted for specimen at a site. Twenty-eight of our original 135 sites passed these selection criteria (see Supporting Table S2).

### 3.2 Paleodirection

The results of the demagnetization experiments vary from multiple unstable directions (e.g., Figure 5a,b,c) to a single stable direction (e.g., Figure 5 d,e). Multiple directions with distinct coercivity and blocking temperature spectra decay along one direction at low field and temperature treatments then abruptly shift to decay along a different direction for the final, characteristic, remanent magnetization (ChRM) (Figure 5a,b). The low temperature or low coercivity component may result from a viscous remanent magnetization or a partial overprint that is typically removed after the first or second treatment. Multiple components with overlapping blocking temperature spectra appear as zig-zagging or gradual shifts in the demagnetization curve (Figure 5c). Zig-zagging may result from tails, if the thermal demagnetization data was derived from an IZZI experiment. We observe gradual changes in the magnetization direction where there may be multiple directional components that are removed in different proportions between each treatment step. We applied a set of criteria (Table 3.2) to select the final stable component of the demagnetization vector, the ChRM. At the specimen level, at least 4 demagnetization steps were used to determine the ChRM and MAD and DANG were set to  $5^\circ$  to constrain the direction. Lawrence et al. (2009) used site level thresholds of  $N > 4$  and  $\kappa > 50$  as acceptance criteria. To ensure consistent directions within a site, we required at least 6 samples per site (N) to calculate the site average direction and set the minimum threshold for  $\kappa$  (Fisher, 1953), a precision parameter to quantify the dispersion in the directions, to 100. One-hundred and eleven sites yield reliable paleodirections (Table 4).

MAD	DANG	N	k
$\leq 5^\circ$	$\leq 5^\circ$	$\geq 6$	$\geq 100$

**Table 2.** Selection criteria applied to our directional data: MAD = maximum angle of deviation, DANG = deviation angle, N = minimum cores per site, k = precision parameter

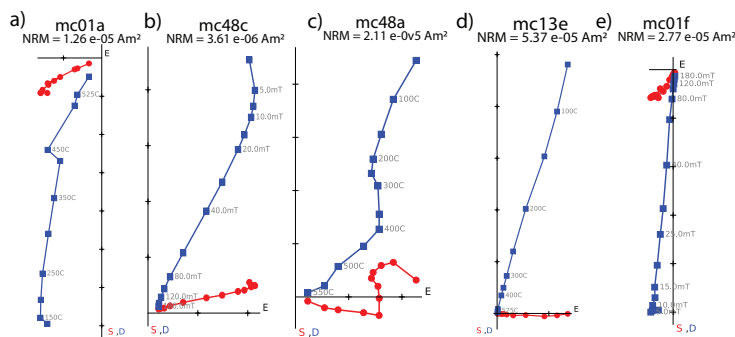


**Figure 5.** Representative Zijderveld diagrams of the directional behaviors observed in our specimens. The projection of the demagnetization vector onto the vertical plane is marked in blue and the projection of the same vector onto the horizontal plane is marked in red. a) Two reverse directions with distinct blocking temperature spectra. A low temperature direction is removed  $0 - 300^\circ$  and a higher temperature component demagnetizes between  $400^\circ - 600^\circ$ . b) Two normal directions with distinct coercivity spectra. The low coercivity component is removed between  $0 - 10$  mT. c) An unstable normal direction from a thermal demagnetization experiment. The specimen may include several directions with overlapping blocking temperature spectra. d) A single stable normal direction from a thermal demagnetization experiment e) A single stable reverse direction from an AF demagnetization experiment.

350

### 3.3 Hysteresis and FORCs

351  
352  
353  
354  
355  
356  
357

Several sites (mc1030, mc1032, mc1115, mc11121, mc1147, and mc1157) passed CCRIT and included estimates from samples that were collected from both the interior (Lawrence et al., 2009) and surface of the same lava flow (this study). At sites mc1030, mc1115, mc1147, and mc1157, the estimates from the interior are  $2\mu T - 8\mu T$  lower than the paleointensity estimates from the lava flow tops (Figure 6). We selected sister specimen for hysteresis loops and FORCs (Harrison & Feinberg, 2008) to examine the domain state or magnetic interactions that may explain the difference.

358  
359  
360  
361  
362

Although each sister specimen passed CCRIT, the specimens exhibit a mixture of magnetic components in the FORCs. We interpret the horizontal ridge in the FORC diagram near  $B_u = 0$  mT (Figure 7) as the contribution from single domain grains after Roberts and Verosub (2000) and Pike et al. (2001). The distribution of coercivities ( $B_c$ ) ranges from 0 to 50 mT and peaks between 0 and 20 mT. This peak is offset from

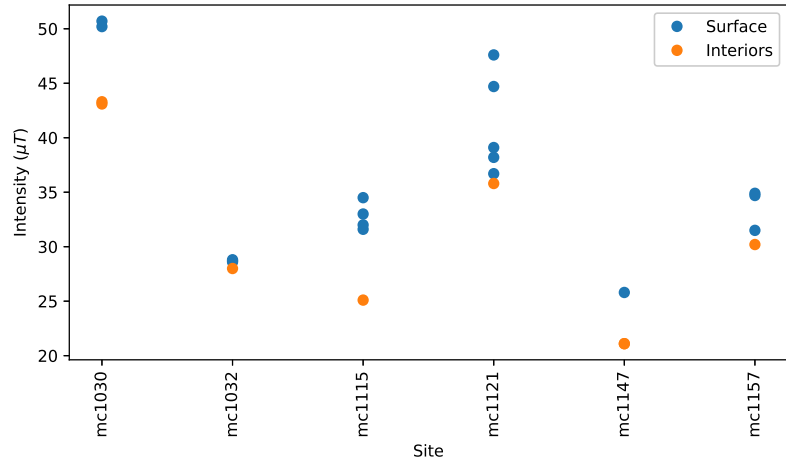


**Figure 6.** Paleointensity estimates from sites that pass CCRIT and include data from both the lava flow top (blue circles) and the lava flow interior (orange circles).

the  $B_u = 0$  mT axis. The contours are shifted downward from this ridge, which reflects the level of interaction fields between the single domain grains. Each specimen displays superparamagnetic behavior as inferred from the vertical ridge near  $B_c = 0$  mT that peaks around  $B_u = 0$  mT.

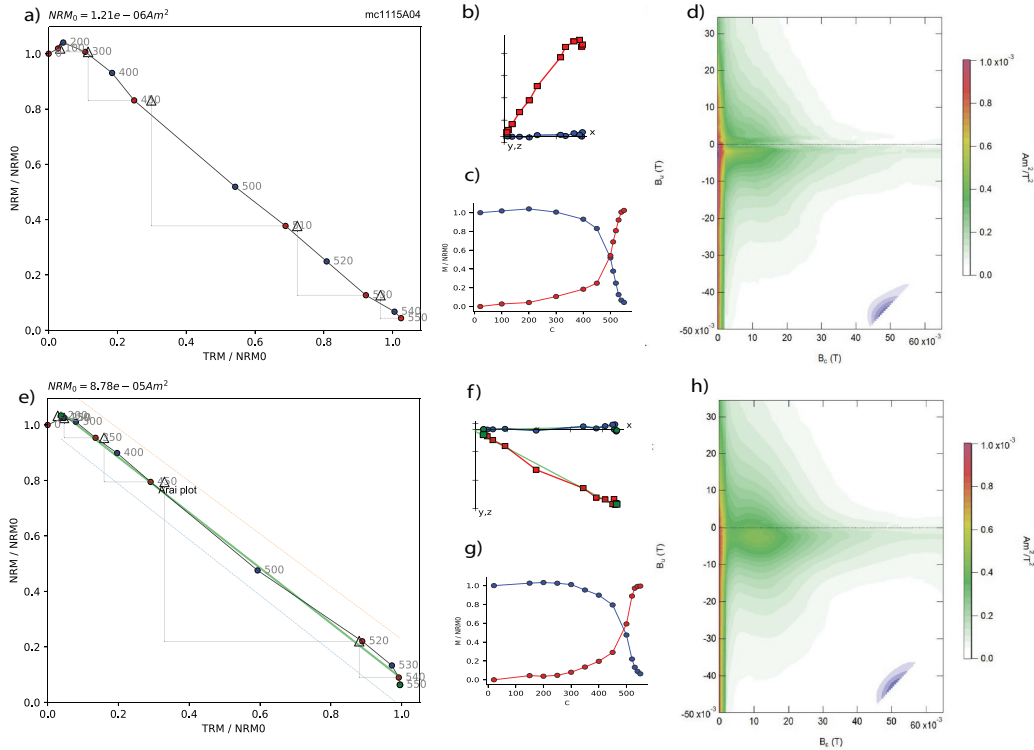


**Figure 7.** Arai diagram (a,e), Zijderveld diagram (b, f), MT curve (c,g), and FORC diagrams (d,h) for samples from site mc1115 that passed CCRIT. Specimen mc1115A04 (a-d) was sampled from the lava flow top and yielded a 31.55 μT paleointensity while mc115a2 (e-h) was collected from the lava flow interior and estimated a 25.15 μT paleointensity

### 367 3.4 $^{40}\text{Ar}/^{39}\text{Ar}$ Geochronology

368 We present thirteen new  $^{40}\text{Ar}/^{39}\text{Ar}$  age analysis from the Erebus Volcanic Province  
 369 (see supporting information Table S2). Site ages were determined by their plateau age.  
 370 Each plateau age estimate includes over 60% of the  $^{39}\text{Ar}_k$  released, excluding sites mc1034,  
 371 mc1131, and mc1157 which only include 52%, 50%, and 44% of the  $^{39}\text{Ar}_k$  released, re-  
 372 spectively (Figure 8). Samples give plateau ages that are concordant with their inverse  
 373 isochron ages. Two samples from site mc1033 yield significantly different age estimates,  
 374 so we exclude both.

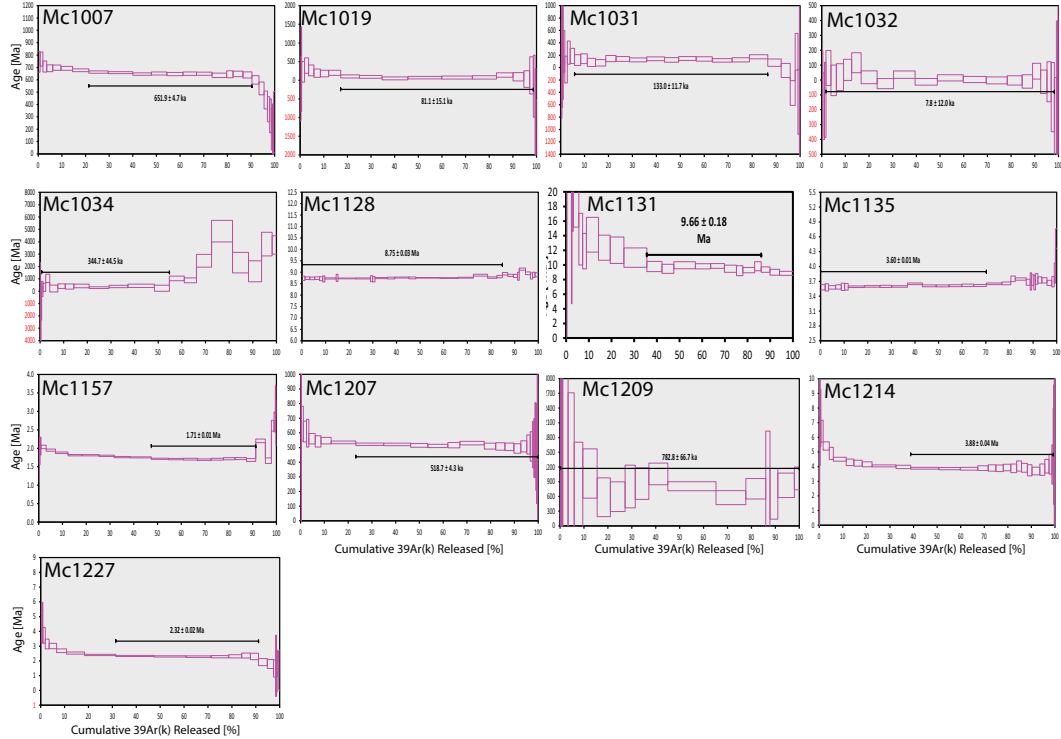


**Figure 8.** Results from the  $^{40}\text{Ar}/^{39}$  incremental heating method used to date 13 sites. Black bars mark the bounds of the age spectra plateau that were used to estimate the site age.

## 375 4 Discussion

### 376 4.1 Examining the GAD structure of the ancient magnetic field

#### 377 4.1.1 Paleointensities

378 Our new paleointensity dataset consists of 28 sites that pass CCRIT. We converted  
 379 the paleointensities to their corresponding virtual axial dipole moments (VADMs) to com-  
 380 pare intensity estimates across latitudes (Table 3). VADM is the strength of the axial  
 381 dipole moment that would generate the intensity observed at a given latitude. Our 28  
 382 sites yield a median intensity of  $33.01 \mu\text{T} \pm 2.59 \mu\text{T}$  or equivalently a median paleomag-  
 383 netic axial dipole moment (PADM) of  $43.40 \text{ ZAm}^2 \pm 3.41 \text{ ZAm}^2$ . Our median intensity  
 384 estimate is slightly higher than that of Lawrence et al. (2009) and about half of the mod-  
 385 ern intensity measured in the Erebus Volcanic Province ( $\sim 62 \mu\text{T}$ ). This is consistent with  
 386 predictions of an average dipole moment of  $\sim 42\text{-}50 \text{ Am}^2$  (e.g., Juarez et al. (1998); Selkin  
 387 and Tauxe (2000); Tauxe et al. (2013); Wang et al. (2015)) over the long term. However,  
 388 there remains the problem that the data from the last few million years from the global  
 389 dataset show no dependence of field strength on latitude (Figure 2) which, if true, be-  
 390 lies the existence of a single geocentric axial dipole moment sampled by all the studies.

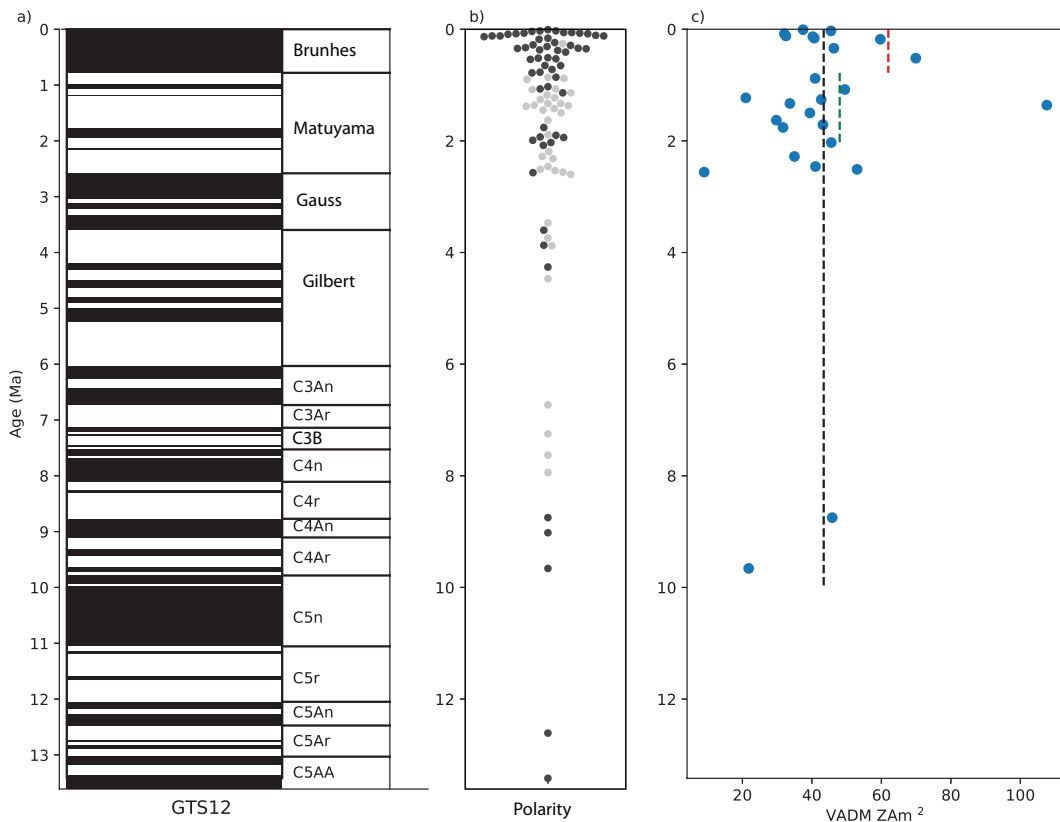


**Figure 9.** a) The 2012 Geomagnetic Polarity Timescale for the Late Neogene (Gradstein et al., 2012). b) The distribution of ages for our sites, colored by normal (black) and reverse (white) polarity. c) The distribution of VADM computed in this study. Red (green) dashed lines are PADM from Zeigler et al. (2011) for the Brunhes and Matuyama (<2 Ma) respectively. Dashed black line is the average PADM for this study.

To assess the structure of the paleomagnetic field over the Late Neogene, we compare our results to globally distributed paleointensity data stored in the PINT database of Biggin et al. (2009). While our estimated PADM of  $43.40 \text{ ZAm}^2 \pm 3.41 \text{ ZAm}^2$  is consistent with many recent estimates for the long term average (e.g., (Juarez et al., 1998; Selkin & Tauxe, 2000; Ziegler et al., 2011; Tauxe et al., 2013; Wang et al., 2015)), our intensity estimate at the high southerly latitudes, when compared to the global data set, does not display the latitudinal dependence of intensity expected of a GAD generated field (Figure 2) and appears depressed when compared to the global paleointensity dataset over the Late Neogene.

The apparent discrepancy between our results and the global dataset could result from a PADM of  $\sim 45 \text{ ZAm}^2$ , which is substantially weaker than the modern dipole moment of  $\sim 77 \text{ ZAm}^2$ . However, we would expect to recover even lower intensities at lower latitude sites ( $\sim 15 \mu\text{T}$  at the equator) from this weaker dipole. Although a few recent studies (Wang et al., 2015) have published results in agreement with this prediction, many older studies from mid and low latitudes have much higher values (Figure 2) than predicted by a PADM of  $\sim 40 - 50 \text{ ZAm}^2$ .

The reasons for the lack of a dipole signal in the global dataset are not clear. The results from some experimental protocols may be biased (e.g., Cromwell, Trusdell, et al.

Site	Lat(°)	Lon (°)	VADM (ZAm <sup>2</sup> )	n	Intensity ( $\mu$ T)	Age (Ma)
mc1004	-77.84	166.69	46.33	3	35.23	0.34 ± 0.01
mc1015	-77.46	169.21	33.66	3	25.57	1.33 ± 0.02
mc1019	-77.88	165.30	32.08	3	24.40	0.0811 ± 0.0151
mc1029	-78.31	164.79	59.70	7	45.46	0.18 ± 0.08
mc1030	-78.34	164.88	61.49	4	46.82	
mc1031	-78.35	164.30	40.27	3	30.67	0.133 ± 0.0117
mc1032	-78.35	164.30	37.46	4	28.52	0.0078 ± 0.012
mc1035	-78.39	164.24	32.52	3	24.77	0.12 ± 0.02
mc1109	-78.28	163.54	42.69	3	32.50	1.26 ± 0.04
mc1115	-78.24	162.96	41.04	5	31.24	2.46 ± 0.31
mc1117	-78.24	162.97	34.98	4	26.62	2.28 ± 0.24
mc1119	-78.24	162.96	49.49	4	37.67	1.08 ± 0.22
mc1120	-78.24	163.09	31.70	3	24.13	1.76 ± 0.05
mc1121	-78.23	162.95	53.00	6	40.35	2.51 ± 0.06
mc1128	-78.21	166.57	45.85	3	34.90	8.75 ± 0.03
mc1131	-78.21	166.57	21.81	5	16.60	9.66 ± 0.18
mc1139	-78.26	163.08	40.94	3	31.17	0.88 ± 0.08
mc1140	-78.28	163.00	45.58	3	34.70	2.03 ± 0.09
mc1142	-77.85	166.68	20.98	4	15.95	1.23 ± 0.02
mc1147	-78.20	162.96	29.78	3	22.67	1.63 ± 0.34
mc1155	-77.70	162.25	39.42	3	29.97	1.5 ± 0.05
mc1157	-77.70	162.26	43.18	4	32.83	1.71 ± 0.01
mc1164	-77.51	169.33	107.63	3	81.77	1.36 ± 0.01
mc1167	-77.49	169.29	58.49	3	44.43	
mc1207	-77.68	166.52	69.91	3	53.13	0.5187 ± 0.0043
mc1217	-77.51	167.44	40.70	5	30.92	0.16 ± 0.01
mc1218	-77.56	166.98	45.48	5	34.56	0.03 ± 0.01
mc1306	-77.70	162.69	9.00	3	6.84	2.56 ± 0.13

**Table 3.** Successful paleointensity results from this study. VADM: virtual axial dipole moment (ZAm<sup>2</sup>), Intensity: paleointensity ( $\mu$ T), n: samples.

(2018); Cai et al. (2017)). Bias in temporal sampling toward the present could also cause a high bias in the median intensity as more recent data appear to have higher intensities (Selkin & Tauxe, 2000; Ziegler et al., 2011). Sampling material may also affect paleointensity estimates. (Selkin & Tauxe, 2000) recovered the expected latitudinal dependence of paleointensity, with a PADM of  $\sim$ 45 ZAm<sup>2</sup>, by examining paleointensities solely from submarine basalt glass. Therefore, in the following section we explore the effect of sampling material on the resulting paleointensity estimate.

#### 4.2 Examining the role of sampling material

In Figure 10 we compare results from our sites that passed CCRIT with the original interpretations of Lawrence et al. (2009). A few sites (mc1147, mc1155, and mc1035) yield similar intensity estimates while others vary by 2 - 15  $\mu$ T. Six of the original sites have specimens that passed CCRIT and include specimens from both the interior and the surface of the same lava flow. We assume that a single lava flow cooled quasi-instantaneously, so the surface and interior of the flow should preserve identical intensities. However, at these sites (Figure 6), specimens from the interior yield systematically lower paleointensities than those from the flow top by 2  $\mu$ T - 8  $\mu$ T.

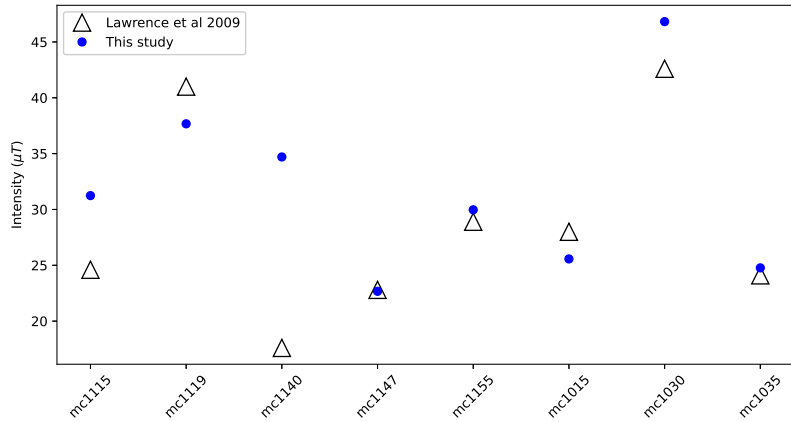


**Figure 10.** Average intensity estimates for the sites in this study that passed CCRIT (blue dots) and the sites from Lawrence et al. 2009 (white triangles) that passed their set of selection criteria.

A slower cooling rate may result in a higher intensity of magnetization (Dodson and McClelland-Brown (1980); Santos and Tauxe (2019)) so we tested the effect of cooling rate on the TRM of the specimens by conducting a cooling rate experiment. Each specimen preserved a higher remanence following slow cooling than fast cooling as expected from SD theory (see supporting information Figure S5). Therefore differences in the cooling history between the two sampling regions (i.e. that the flow tops cooled more quickly than the flow interiors) does not explain the lower paleointensities we measure in the interior, if they are both single domain.

Next, we tested whether differences in domain state or magnetic interaction could explain the behavior by measuring hysteresis loops and FORC diagrams (Pike et al., 1999). The magnetic moments in specimens from mc1115 (Figure 7) and mc1147 (see supporting information Figure S6) include a superparamagnetic component, a single domain component and some degree of interaction (Roberts & Verosub, 2000), but the domain structure of specimens from the interiors appears broadly similar to those from the flow tops at the same site for the specimens that passed CCRIT tested here. Therefore, differences in domain states do not account for the higher paleointensities measured in the samples collected from the surface.

In addition to cooling rate and domain state, we investigated whether non-linear TRM acquisition could explain the bias in the intensity estimates from the interior. Our samples, collected from the surface during the 2016/2017 field season, were treated in a  $30 \mu T$  field during the in-field steps of the IZZI experiment. Lawrence et al. (2009) cooled some specimens from the interior in a  $25 \mu T$  field and other specimens in a  $30 \mu T$  field. To test for non-linearity, we performed TRM acquisition tests in fields from 0 to  $60 \mu T$  to investigate whether the lower intensities measured in the interiors resulted from the lower intensities applied during the IZZI experiment (Supporting information Figure S7). All specimens showed linear behavior with applied field. Thus, neither cooling rate, domain state, nor non-linear TRM acquisition accounts for the lower intensities recorded by the specimens sampled from the interior of the lava flows. Only six of our 28 successful sites include paleointensity estimates from both the surface and the interior. We believe the intensity estimates that pass CCRIT from both contexts preserve reliable intensity estimates. A full investigation on the role of sampling material on paleointensity estimates would require a larger sample size.

457 **4.2.1 Paleodirections**

458 **4.2.1.1 Paleopole** We have compiled our new directional data with the data of  
 459 Lawrence et al. (2009) (see supporting Table S1 for combined sites) and (re)analyzed all  
 460 of the directional data. Our new dataset consists of 107 site-mean directions that pass  
 461 our (stricter) selection criteria (Table 4). It includes 66 normal polarity (Figure 11a) and  
 462 41 reverse polarity (Figure 11b) site-mean directions (Table 5). We applied a bootstrap  
 463 reversal test (Tauxe et al., 1991) on the reverse and normal directions. The directions  
 464 pass the reversal test, so the two sets are indistinguishable (see supporting information  
 465 Figure S2) and we can combine the antipodes of the reverse directions with the normal  
 466 directions and analyze the combined dataset.

Site	k	N	Dec (°)	Inc (°)	$\alpha_{95}$ (°)	VGP Lat (°)	VGP Lon (°)	Lat (°)	Lon (°)	Age (Ma)
mc1001	356	6	255.3	79.7	3.55	69.49	275.43	-77.85	166.64	$1.18 \pm 0.01$
mc1002	290	6	334.4	-79.1	3.93	78.61	114.74	-77.85	166.69	$0.33 \pm 0.02$
mc1008	361	8	39.4	-77.6	2.92	73.85	233.48	-77.80	166.83	$0.65 \pm 0.05$
mc1009	192	8	253.8	-82.8	4.00	68.81	26.53	-77.55	166.20	$0.07 \pm 0.02$
mc1010	217	7	335.9	-77.6	4.11	76.61	120.83	-77.57	166.23	
mc1011	452	8	325.2	-76.8	2.61	73.59	107.24	-77.57	166.23	
mc1014	450	8	0.5	-80.6	2.61	84.16	170.66	-77.46	169.23	
mc1015	949	9	172.2	84.6	1.67	87.61	26.42	-77.47	169.23	$1.33 \pm 0.02$
mc1020	128	7	137.9	-79.3	5.34	59.24	317.40	-77.88	165.02	$0.77 \pm 0.032$
mc1021	301	8	333.1	80.5	3.20	60.56	329.58	-78.21	166.49	
mc1029	106	6	25.2	-78.5	6.52	77.47	212.51	-78.31	164.80	$0.18 \pm 0.08$
mc1030	140	8	242.5	68.8	4.69	56.23	242.70	-78.34	164.87	
mc1032	168	7	266.1	-75.3	4.66	59.48	49.92	-78.36	164.30	$0.0078 \pm 0.012$
mc1033	381	8	9.6	-74.5	2.84	72.39	179.81	-78.38	164.34	
mc1034	393	7	281.6	-82.2	3.05	72.85	45.41	-78.39	164.27	$0.3447 \pm 0.0445$
mc1035	316	8	301.6	-84.7	3.12	79.22	40.38	-78.39	164.23	$0.12 \pm 0.02$
mc1036	171	7	348.7	-82.2	4.63	85.40	123.78	-78.39	164.27	$0.12 \pm 0.02$
mc1037	316	8	215.6	81.6	3.12	80.27	242.85	-78.40	164.27	$4.47 \pm 0.04$
mc1038	227	7	295.7	-77.9	4.02	69.23	71.27	-78.40	164.21	
mc1039	371	7	282.7	-87.3	3.14	78.34	11.16	-78.39	164.21	$0.08 \pm 0.01$
mc1040	215	7	194.4	-83.0	4.12	64.85	352.17	-78.39	164.20	
mc1041	144	6	270.5	-78.3	5.59	64.85	48.78	-78.39	164.20	$0.28 \pm 0.02$
mc1043	104	6	280.5	-85.1	6.57	76.31	28.83	-78.37	164.24	
mc1044	161	8	325.2	-74.1	4.37	68.86	112.55	-78.36	164.26	
mc1048	229	6	75.8	-54.9	4.43	37.46	247.79	-78.24	163.36	
mc1100	163	6	12.6	-74.3	5.26	71.94	182.97	-78.30	162.90	$0.86 \pm 0.23$
mc1101	863	6	35.8	-79.1	2.28	76.69	228.48	-78.31	162.93	$1.07 \pm 0.01$
mc1103	220	7	136.7	71.2	4.07	63.25	104.41	-78.24	163.36	$1.42 \pm 0.03$
mc1104	236	6	69.0	-75.5	4.37	64.56	256.04	-78.24	163.40	$0.29 \pm 0.02$
mc1106	434	6	18.4	-76.3	3.22	74.72	194.98	-78.21	163.31	$13.42 \pm 0.18$
mc1107	783	6	95.5	-84.5	2.40	73.27	302.68	-78.20	163.35	$2.57 \pm 0.38$
mc1109	661	6	172.6	76.0	2.61	74.98	150.65	-78.28	163.54	$1.26 \pm 0.04$
mc1110	245	6	253.4	80.0	4.28	70.49	270.66	-78.24	163.44	$7.94 \pm 0.24$
mc1111	1193	7	47.9	-67.8	1.75	57.63	224.04	-78.22	162.79	$1.99 \pm 0.04$
mc1112	159	6	232.9	74.4	5.31	66.17	237.62	-78.24	163.44	$7.63 \pm 0.32$
mc1113	130	7	257.0	77.6	5.30	66.13	266.80	-78.23	162.74	$6.73 \pm 0.17$
mc1115	222	6	74.9	67.5	4.50	46.10	45.51	-78.24	162.96	$2.46 \pm 0.31$
mc1116	157	6	275.6	-80.7	5.36	69.44	44.86	-78.22	162.74	$1.14 \pm 0.11$
mc1117	1152	6	169.0	68.9	1.97	63.85	147.72	-78.24	162.97	$2.28 \pm 0.24$
mc1118	108	7	58.6	-52.2	5.82	38.27	229.23	-78.24	163.14	$0.31 \pm 0.04$
mc1119	966	6	126.3	48.4	2.16	35.80	102.92	-78.24	162.96	$1.08 \pm 0.22$

Continued on next page

Site	k	N	Dec (°)	Inc (°)	$\alpha_{95}$ (°)	VGP Lat (°)	VGP Lon (°)	Lat (°)	Lon (°)	Age (Ma)
mc1120	624	9	72.4	-70.5	2.06	56.59	252.58	-78.24	163.09	1.76 ± 0.05
mc1121	641	10	117.8	79.1	1.91	71.47	68.16	-78.24	162.95	2.51 ± 0.06
mc1123	296	8	75.8	-82.5	3.22	73.59	282.42	-78.25	163.73	1.93 ± 0.05
mc1124	385	6	15.2	-72.7	3.42	69.26	186.58	-78.19	163.57	12.61 ± 0.11
mc1125	153	7	342.6	-63.7	4.89	56.39	141.47	-78.25	163.73	4.26 ± 0.18
mc1126	305	7	12.7	-77.9	3.46	77.99	188.33	-78.25	163.74	
mc1127	689	8	325.3	-66.9	2.11	58.62	118.62	-78.25	163.73	1.94 ± 0.07
mc1128	370	8	33.4	-80.8	2.88	79.67	237.79	-78.21	166.57	8.75 ± 0.03
mc1130	257	6	150.1	46.3	4.18	37.66	132.63	-78.21	166.58	7.25 ± 0.07
mc1131	398	8	20.8	-58.6	2.78	50.15	192.03	-78.21	166.57	9.66 ± 0.18
mc1133	305	6	38.8	-85.6	3.84	82.63	298.22	-78.20	166.58	
mc1134	1049	6	11.8	-84.2	2.07	87.60	267.63	-78.22	166.61	9.02 ± 0.05
mc1135	209	8	266.3	-77.6	3.83	62.95	48.78	-78.23	166.56	3.6 ± 0.01
mc1139	892	6	169.8	79.0	2.24	80.05	141.19	-78.26	163.08	0.88 ± 0.08
mc1140	553	6	343.7	-78.7	2.85	79.03	129.91	-78.28	163.00	2.03 ± 0.09
mc1141	100	6	91.4	83.4	6.71	72.36	150.00	-77.58	-77.58	1.31 ± 0.02
mc1142	355	9	318.5	85.3	2.73	69.82	328.38	-77.85	166.68	1.23 ± 0.02
mc1143	188	6	29.8	-52.1	4.90	42.70	197.51	-78.24	162.88	2.08 ± 0.65
mc1144	108	7	198.4	79.6	5.83	80.63	208.42	-77.85	166.69	
mc1145	773	6	27.6	2.6	2.41	9.12	190.86	-78.24	162.89	1.9 ± 0.12
mc1146	122	7	236.1	63.2	5.48	50.34	230.48	-78.22	162.96	1.37 ± 0.42
mc1147	361	6	220.3	64.3	3.53	54.44	213.47	-78.20	162.96	1.63 ± 0.34
mc1148	104	6	283.6	-79.6	6.58	69.09	56.82	-77.49	167.25	0.72 ± 0.66
mc1152	887	6	333.2	-85.6	2.25	84.02	23.24	-77.72	162.65	3.87 ± 0.15
mc1153	161	6	311.2	57.9	5.29	29.98	299.36	-77.76	162.14	2.53 ± 0.13
mc1154	514	6	283.1	87.7	2.96	75.98	324.02	-77.72	162.63	2.19 ± 0.08
mc1155	212	8	230.1	78.1	3.81	72.47	243.37	-77.70	162.25	1.5 ± 0.05
mc1156	381	6	162.7	72.7	3.43	69.56	135.88	-77.70	162.59	1.89 ± 0.13
mc1158	971	6	48.6	43.7	2.15	17.07	27.60	-77.69	162.46	3.74 ± 0.25
mc1160	214	8	233.5	77.8	3.79	71.23	245.95	-77.69	162.35	3.47 ± 0.05
mc1164	1255	7	201.6	85.6	1.70	84.59	312.77	-77.51	169.33	1.36 ± 0.01
mc1165	151	6	159.2	79.6	5.45	80.45	121.68	-77.51	169.33	1.45 ± 0.06
mc1167	6080	8	186.2	72.5	0.71	70.11	179.11	-77.49	169.29	
mc1168	197	7	183.7	67.7	4.30	63.16	174.45	-77.49	169.29	1.38 ± 0.05
mc1170	1621	6	2.2	-87.5	1.66	82.76	345.19	-77.85	166.71	1.03 ± 0.1
mc1200	342	6	301.9	-84.8	3.62	78.81	38.42	-77.55	166.16	0.07 ± 0.01
mc1201	347	6	257.4	-79.7	3.60	64.35	36.72	-77.56	166.22	0.09 ± 0.01
mc1202	3487	6	341.2	-46.6	1.13	39.48	144.75	-77.66	166.36	0.54 ± 0.01
mc1205	579	9	283.4	-34.2	2.14	21.20	85.69	-77.66	166.73	0.37 ± 0.02
mc1206	147	9	326.2	-32.6	4.26	27.79	129.99	-77.67	166.78	
mc1207	334	6	46.0	-71.2	3.67	62.99	229.63	-77.68	166.52	0.5187 ± 0.0043
mc1208	256	6	38.3	-66.2	4.19	57.45	216.21	-77.67	166.53	
mc1209	473	6	59.2	-62.7	3.08	49.29	237.50	-77.69	166.37	0.7828 ± 0.0667
mc1210	1141	6	51.6	-69.4	1.98	59.36	233.89	-77.69	166.37	
mc1211	617	8	4.8	-55.5	2.23	48.36	172.17	-77.66	166.34	
mc1214	1575	10	176.2	77.8	1.22	79.35	158.17	-77.22	166.43	3.88 ± 0.04
mc1215	268	8	347.8	-82.4	3.38	86.26	110.24	-77.48	166.89	0.34 ± 0.02
mc1217	114	10	287.0	-71.9	4.54	58.43	74.76	-77.51	167.44	0.16 ± 0.01
mc1218	132	6	343.4	-81.5	5.84	84.10	114.26	-77.56	166.98	0.03 ± 0.01
mc1220	391	10	36.8	-82.4	2.44	81.15	260.37	-77.46	166.91	0.53 ± 0.04
mc1221	454	6	274.1	-82.9	3.15	72.06	37.94	-77.52	166.80	0.12 ± 0.01
mc1222	307	6	190.4	-52.1	3.83	20.45	356.14	-77.54	166.85	0.11 ± 0.01

Continued on next page

Site	k	N	Dec (°)	Inc (°)	$\alpha_{95}$ (°)	VGP Lat (°)	VGP Lon (°)	Lat (°)	Lon (°)	Age (Ma)
mc1223	161	9	59.8	-82.6	4.06	76.53	277.72	-77.66	166.79	0.38 ± 0.03
mc1224	568	6	192.0	-61.0	2.81	29.86	357.10	-77.53	166.88	0.03 ± 0.01
mc1225	1052	6	113.8	-74.6	2.07	54.46	297.40	-77.58	166.80	0.06 ± 0.01
mc1226	1468	6	19.3	-50.6	1.75	42.93	189.46	-77.61	166.77	0.24 ± 0.02
mc1227	2347	6	221.2	61.8	1.38	51.92	218.00	-77.27	166.73	2.32 ± 0.02
mc1228	161	10	212.2	67.7	3.81	60.68	210.15	-77.27	166.38	
mc1229	339	8	99.5	73.1	3.01	58.57	65.93	-77.48	167.15	1.07 ± 0.18
mc1301	707	6	134.2	77.4	2.52	72.13	209.25	-78.22	-78.22	
mc1302	368	11	102.5	-73.9	2.38	55.68	41.92	-78.19	-78.19	0.04 ± 0.01
mc1303	263	17	17.8	-55.1	2.20	47.33	303.94	-77.58	-77.58	1.31 ± 0.02
mc1304	198	13	156.5	75.6	2.95	73.03	243.19	-78.24	-78.24	0.29 ± 0.02
mc1305	482	16	191.3	71.1	1.68	67.07	298.26	-78.24	-78.24	0.9 ± 0.1
mc1306	175	12	171.4	57.1	3.28	49.81	271.69	-77.70	-77.70	2.56 ± 0.13
mc1307	367	18	226.1	75.5	1.81	69.34	351.67	-77.85	-77.85	1.33 ± 0.12

Table 4: Successful paleodirection results:  $\kappa$ : precision parameter, N: cores per site, Dec: declination (°), Inc: inclination (°),  $\alpha_{95}$ : Circle of 95% confidence, VGP Lat: virtual geomagnetic pole latitude (°), VGP Lon: virtual geomagnetic pole longitude (°), Lat: site latitude, Lon: site longitude, Age = age (Ma). Site names were modified for this study. Sites from Mankinen and Cox (1988) (mc1-50) are renamed mc1001-mc1050 while those from Lawrence et al. (2009) (mc100-mc229) are renamed mc1100-mc1229. Sites that were recombined for this study are labeled mc1301-mc1307.

A VGP is the coordinates of the geocentric magnetic dipole that would generate the direction measured at a particular location. The paleomagnetic site-mean directions were transformed to their corresponding virtual geomagnetic poles (VGPs) (Figure 11d-f). We calculated the paleomagnetic pole and  $\alpha_{95}$  (Fisher, 1953) by taking the average of the VGPs for the normal polarity sites in Figure 11d ( $176.8^\circ$ ,  $87.5^\circ$ , and  $\alpha_{95} 6.8^\circ$ ), the antipode of the reverse polarity sites in Figure 11e, ( $232.7^\circ$ ,  $85.6^\circ$ , and  $\alpha_{95} 9.5^\circ$ ) and for the combined dataset in Figure 11f ( $205.6^\circ$ ,  $87.1^\circ$ , and  $\alpha_{95} 5.5^\circ$ ), see Table 5. The 95% confidence bounds of each paleopole includes the spin axis, so the paleodirections from our study are consistent with a GAD field.

Polarity	N	Dec (°)	Inc (°)	VGP lon (°)	VGP lat (°)	$\alpha_{95}$ (°)
Normal Intervals	66	4.6	-81.1	176.8	87.5	6.8
Reverse Intervals	41	179.2	82.0	232.7	85.6	9.5
Combined	107	2.7	-81.5	205.6	87.1	5.5

**Table 5.** Paleodirectional results from this study. N: number of sites, Dec: declination, Inc: inclination, VGP lon: VGP longitude, VGP lat: VGP latitude,  $\alpha_{95}$ : 95% confidence bounds.

**4.2.1.2 VGP Dispersion** In addition to testing the GAD hypothesis by comparing the paleopole from this study with the coordinates of the spin axis, we can test the variability of the geomagnetic field, paleosecular variation (PSV), over the Late Neogene by calculating the dispersion of the VGPs about the geographic pole (McElhinny, 1973). VGP dispersion quantifies the scatter in the site-level VGP estimates. The scatter within each site will vary based on the directions selected to calculate the VGP. At the site-level, we follow Behar et al. (2019) in setting the number of cores per site (N) to  $\geq 6$  and the precision parameter (k) to  $\geq 100$  as our criteria to minimize VGP dispersion without discarding too many sites, N, that fail to meet these criteria (Table 4). Although the within-

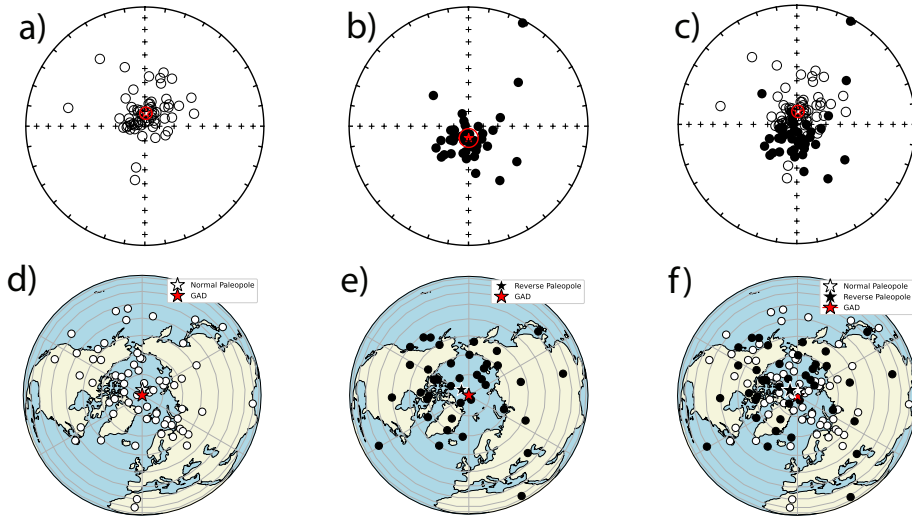


**Figure 11.** a-c) Equal area projections of the site mean directions that passed our selection criteria along with their corresponding  $\alpha_{95}$ s (red circles). Upward (lower) hemisphere projections are open (closed) circles. a) normal polarity directions b) reverse polarity directions and c) all directions. d-e) Maps of the VGPs (circles). The paleopole for each interval is marked with a white star and the GAD as a red star. The  $\alpha_{95}$ s around the paleopoles are marked as red circles. d) the normal interval (directions in a), e) the reverse interval (directions in b), and f) the entire dataset (directions in c); the reverse data (black circles) are flipped to the antipode.

site scatter differs between sites, we assume that the N and k cut-offs account for this variability, and so we quantify VGP dispersion using S (Cox, 1970):

$$S^2 = (N - 1)^{-1} \sum_{i=1}^N (\Delta_i)^2 \quad (5)$$

where N is the number of sites and  $\Delta_i$  is the angular deviation between the  $i^{th}$  VGP and the spin axis. We calculate  $S_p$  for the normal poles, the reverse poles, and the combined dataset which includes the antipode of the reverse poles and the normal poles that passed our set of selection criteria (Table 6). We also calculate the 95% bootstrap upper and lower confidence bounds for the VGP dispersion of each dataset. The VGP dispersion is higher for the normal poles than the reverse poles but both results fall within the overlapping 95% bootstrap confidence bounds of the two datasets so the difference in VGP dispersion is insignificant.

For  $S_{45}$ , we filter the VGPs that passed our selection criteria by applying a strict  $45^\circ$  VGP cut-off. The rationale for applying cutoffs is that VGPs with low latitudes may reflect directions acquired during transitional or excursionial field states. These directions record an unstable geomagnetic field state so VGP cut-offs were introduced to exclude these from the calculation of dispersion (Watkins, 1973). Applying a  $45^\circ$  VGP cut-off, reduces dispersion by  $5 - 8^\circ$ . The VGP dispersion is higher in the reverse poles than the normal poles, but once again the poles fall within their overlapping 95% bootstrap confidence bounds so the difference is not significant. Although a VGP cut-off may remove transitional/excursional field directions, it may also underestimate dispersion by excluding ‘normal’ secular variation. For example, a strict  $45^\circ$  VGP cut-off would bias against

494 paleodirections recovered from high latitudes because there is a latitudinal dependence  
 495 of dispersion- higher latitudes record higher dispersion (McFadden et al., 1988).

496 For  $S_{vand}$  we filter the original VGP dataset with the Vandamme cut-off (Vandamme,  
 497 1994) which applies an iterative VGP cut-off. Applying this VGP filter also reduces the  
 498 VGP dispersion.

499 Our results include paleodirections from the Late Neogene, including many from  
 500 the Brunhes, Matuyama and Gilbert Chrons (see Figure 9). We test whether dispersion  
 501 varies between chronos by filtering our dataset by age and calculating the dispersion and  
 502 95% bootstrap confidence bounds of each separate chronon. Our dataset includes a single  
 503 VGP from the Gauss chron so we exclude this Chron from our calculation. For both fil-  
 504 tered and unfiltered VGPs, the dispersion falls within the overlapping 95% bootstrap con-  
 505 fidence interval (see supporting information Figure S4), so our dataset suggests there is  
 506 no distinction in VGP dispersion between chronons.

	S	$N_S$	$S_{45}$	$N_{S45}$	$S_{vand}$	$N_{Svand}$				
Normal	30.18 26.12	32.88 25.52	66	23.03 20.84	25.81 21.79	57	24.27 21.18	29.99 21.42	20.26	59
Reverse	32.37	38.04 25.52	41	24.37	27.45 21.79	36	24.37	32.45 21.18	28.17	36
Combined	30.88 26.54	33.60 26.38	107	23.42	25.69 21.38	93	24.17	21.42	28.17	95
Brunhes	32.36 26.18	37.19 18.90	31	21.37	24.52 18.90	24	25.98	37.59 18.30	21.42	28
Matuyama	31.15 24.90	35.64 20.29	39	25.40	29.83 20.29	11	26.06	31.99 22.29	22.29	36
Gilbert	30.98 20.52	38.21 16.85	16	24.67	30.56 16.85	8	22.08	39.67 17.00	17.00	14
TK03	23.35 20.29	27.37 20.29	107*	19.68	21.60 18.08	107*	18.76	21.22 16.60	21.22	107*

**Table 6.** S: VGP dispersion,  $S_{45}$ : VGP dispersion for the data filtered by a  $45^\circ$  VGP cut-off, and  $S_{vand}$ : VGP dispersion for the data filtered by the Vandamme cut-off. Beside the VGP dispersion is the bootstrap upper (top) and lower (bottom) 95% confidence bounds for each set of VGPs. \*bootstrapped 1000 times.

507 We compare the results from our dataset to estimates of dispersion from a set of  
 508 directions drawn from a statistical PSV model, TK03 (Tauxe & Kent, 2004). We drew  
 509 a set of directions from the centroid position of our sites ( $78.22^\circ\text{S}$ ,  $164.34^\circ\text{E}$ ), transformed  
 510 the directions to their corresponding VGPs, and then calculated dispersion for the syn-  
 511 thetic dataset. We repeated these steps 1000 times for an  $S$  of  $24.88^{26.30}_{23.13}$ . The disper-  
 512 sion of our  $S_{45}$  and  $S_{vand}$  filtered VGPs are consistent with our unfiltered estimate of  
 513 dispersion from the statistical PSV model TK03. The bounds on the unfiltered VGPs  
 514 overlap with the bootstrapped 95% confidence interval of our TK03 derived dispersion.  
 515 Based on our results, dispersion appears consistent between normal and reverse polar-  
 516 ities, consistent between the Brunhes and Matuyama chron, and consistent with than  
 517 VGP dispersion predicted by TK03 (Tauxe & Kent, 2004). We note however that the  
 518 dispersions for this high latitude study are higher than those predicted by TK03 (although  
 519 within uncertainty) and that other Giant Gaussian Process models (i.e. Bono et al. (2020),  
 520 BB18-family) would provide a better fit.

## 521 5 Conclusions

522 We present an extensive study of the paleomagnetic field over the Neogene in the  
 523 Erebus Volcanic Province, Antarctica ( $-77.84^\circ$ ,  $166.69^\circ$ ) and eleven new  $^{40}\text{Ar}/^{39}\text{Ar}$  re-  
 524 sults. We recovered a paleopole at  $205.6^\circ$ ,  $87.1^\circ$  from 107 independent sites that were  
 525 subjected to both thermal and AF demagnetization and then filtered using a set of strict  
 526 selection criteria. The  $\alpha_{95}$  of the paleopole is  $5.5^\circ$  and encompasses the spin axis so the  
 527 paleodirections measured from the EVP during the Neogene are consistent with a GAD

528 field. Additionally, we conducted an IZZI-modified Thellier-Thellier experiment and ap-  
 529 plied the CCRIT set of selection criteria to estimate paleointensity. Twenty-eight sites  
 530 passed our criteria and recorded a  $33.01 \mu\text{T} \pm 2.59 \mu\text{T}$  median intensity and a  $43.40 \text{ ZAm}^2 \pm$   
 531  $3.41 \text{ ZAm}^2$  median VADM. Compared with global paleointensity estimates stored in the  
 532 PINT database, our results from Antarctica are lower than expected for a purely GAD  
 533 field generated by a dipole with the present data value. We conclude that this lower in-  
 534 tensity near the pole reflects weaker PDM. However, the possibility remains that there  
 535 was a strongly non-GAD structure of the paleomagnetic field over the Late Neogene. To  
 536 test this further, we must repeat this same study of Late Neogene paleomagnetic field  
 537 at several latitudes (Dossing et al., 2016; Wang et al., 2015) to ensure adequate tempo-  
 538 ral overlap and high-quality paleointensity results.

### 539 Acknowledgments

540 This work was funded by the National Science Foundation Grants OPP1541285 and EAR1827263.  
 541 The first author gratefully acknowledges support by the National Science Foundation Grad-  
 542 uate Research Fellowship under Grant No. DGE-1650112. We thank the United States  
 543 Antarctic Program for their ground support in Antarctica. We thank Christeanne San-  
 544 tos for her assistance with data collection and Cathy Constable, Jeff Gee, Shuhui Cai,  
 545 and Nicole Behar for their helpful discussions. The data are available here

546 <https://earthref.org/MagIC/16912/14bee173-cd18-4c33-858e-de5eab74c528>

547 and will be made public at: <https://earthref.org/MagIC/16912> upon acceptance of this  
 548 manuscript.

### 549 References

- 550 Aitken, M. J., Allsop, A. L., Bussell, G. D., & Winter, M. B. (1988). Determina-  
 551 tion of the intensity of the Earth's magnetic field during archeological times:  
 552 reliability of the Thellier technique. *Rev. Geophys.*, *26*, 3–12.
- 553 Behar, N., Shaar, R., Tauxe, L., Asefaw, H., Ebert, Y., Heimann, A., ... Hagai, R.  
 554 (2019). Paleomagnetism and paleosecular variations from the Plio-Pleistocene  
 555 Golan Heights Volcanic Plateau, Israel. *Geochemistry, Geophysics, Geosys-*  
 556 *tems*, *20*, 4319–4334.
- 557 Ben-Yosef, E., Tauxe, L., Levy, T., Shaar, R., Ron, H., & Najjar, M. (2009). Ge-  
 558 omagnetic intensity spike recorded in high resolution slag deposit in southern  
 559 Jordan. *Earth and Planetary Science Letters*, *287*, 529–539.
- 560 Biggin, A. (2010). Paleointensity database updated and upgraded. *EOS*, *91*, 15.
- 561 Biggin, A., Strik, G., & Langereis, C. (2009). The intensity of the geomagnetic field  
 562 in the late-Archean: new measurements and analysis of the updated IAGA  
 563 palaeointensity database. *Earth Planets and Space*, *61*, 9–22.
- 564 Bono, R., Biggin, A., Holme, R., Davies, C., Meduri, D., & Bestard, J. (2020).  
 565 Covariant giant gaussian process models with improved reproduction of pa-  
 566 leosecular variation. *Geochem. Geophys. Geosys.*, *21*, e2020GC008960. doi:  
 567 10.1029/2020GC008960
- 568 Cai, S., Tauxe, L., & Cromwell, G. (2017). Paleointensity from subaerial basaltic  
 569 glasses from the second Hawaii Scientific Drilling Project (HSDP2) core and  
 570 implications for possible bias in data from lava flow interiors. *J. Geophys. Res.*,  
 571 *122*, 8664–8674. doi: 10.1002/2017JB014683
- 572 Coe, R. (1967). Paleo-intensities of the Earth's magnetic field determined from  
 573 Tertiary and Quaternary rocks. *Journal of Geophysical Research*, *72*(12), 3247–  
 574 3262.
- 575 Constable, C., Korte, M., & Panovska, S. (2016). Persistent high paleosecular  
 576 variation activity in southern hemisphere for at least 10,000 years. *Earth and*  
 577 *Planet. Sci. Lett.*, *453*, 78–86.

- 578 Cox, A. (1970). Latitude dependence of the angular dispersion of the geomagnetic  
579 field. *Geophys. J. Roy. Astron. Soc.*, *20*, 253-269.
- 580 Creer, K. (1967). *Thermal demagnetization by the continuous method*. Chapman and  
581 Hall.
- 582 Cromwell, G., Tauxe, L., Constable, C., & Jarboe, N. (2018). PSV10: A global  
583 dataset for 0-10 Ma time-averaged field and paleosecular variation studies.  
*Geochemistry, Geophysics, Geosystems*, *19*, 1533-1558.
- 584 Cromwell, G., Tauxe, L., Staudigel, H., & Ron, H. (2015). Paleointensity estimates  
585 from historic and modern Hawaiian lava flows using basaltic volcanic glass as a  
586 primary source material. *Phys. Earth Planet. Int.*, *241*, 44-56.
- 588 Cromwell, G., Trusdell, F., Tauxe, L., Staudigel, H., & Ron, H. (2018). Holocene pa-  
589 leointensity of the island of Hawai'i from glassy volcanics. *Geochem. Geophys.*  
590 *Geosys.*, *19*, 3224-3245. doi: 10.1002/2017GC006927
- 591 Dodson, M., & McClelland-Brown, E. (1980). Magnetic blocking temperatures of  
592 single-domain grains during slow cooling. *Journal of Geophysical Research*, *85*,  
593 2625-2637.
- 594 Dossing, A., Muxworthy, A., Supakulopas, R., Riishuuus, M., & Mac Niocaill, C.  
595 (2016). High northern geomagnetic field behavior and new constraints on  
596 the Gilsa event: Paleomagnetic and  $^{40}\text{Ar}/^{39}\text{Ar}$ . *Earth and Planetary Science*  
597 *Letters*, *456*, 98-111.
- 598 Dunlop, D., & Özdemir, O. (2001). Beyond Néel's theories: thermal demagnetization  
599 of narrow-band partial thermoremanent magnetization. *Phys. Earth Planet.  
600 Int.*, *126*, 43-57.
- 601 Dunlop, D., Zhang, B., & Özdemir, O. (2005). Linear and nonlinear thellier pale-  
602 ointensity behavior of natural minerals. *Journal of Geophysical Research*, *110*,  
603 B01103. doi: <https://doi.org/10.1029/2004JB003095>
- 604 Fisher, R. A. (1953). Dispersion on a sphere. *Proc. Roy. Soc. London, Ser. A*, *217*,  
605 295-305.
- 606 Fox, J., & Aitken, M. (1980). Cooling-rate dependence of thermoremanent magneti-  
607 sation. *Nature*, *283*, 462-463.
- 608 Gilbert, W. (1958). *On the Magnet, Facsimile of 1900 translation by Silvanus P.  
609 Thompson and the Gilbert Club*. New York: Basic Books, Inc.
- 610 Glatzmaier, G., & Coe, R. (2007). Magnetic polarity reversals in the core. In *Core  
611 dynamics* (Vol. 5, p. 283-297). Elsevier.
- 612 Gradstein, F., Ogg, J., Schmitz, M., & Ogg, G. (2012). *Geologic time scale 2012*.  
613 Amsterdam: Elsevier.
- 614 Halgedahl, S., & Fuller, M. (1980). Magnetic domain observations of nucleation pro-  
615 cesses in fine particles of intermediate titanomagnetite. *Nature*, *288*, 70-72.
- 616 Harrison, R., & Feinberg, J. (2008). An improved algorithm for calculat-  
617 ing first-order reversal curve distributions using locally weighted regres-  
618 sion smoothing. *Geochemistry Geophysics Geosystems*, *9*, Q05016. doi:  
619 doi:10.1029/2008GC001987
- 620 Heaton, D., & Koppers, A. (2019). High-resolution  $^{40}\text{Ar}/^{39}\text{Ar}$  geochronology of  
621 the Louisville Seamounts IODP Expedition 330 drill sites: Implications or the  
622 duration of hot spot-related volcanism and age progressions. *Geochemistry,  
623 Geophysics, Geosystems*, *46*, 4073-4102. doi: 10.1029/2019GL083542
- 624 Hoffman, K., & Biggin, A. (2005). A rapid multi-sample approach to the determina-  
625 tion of absolute paleointensity. *J. Geophys. Res.*, *110*, B12108.
- 626 Holme, R. (2007). Large-scale flow in the core. In *Core dynamics* (Vol. 5, p. 107-  
627 130). Elsevier.
- 628 Irving, E., Robertson, W., Stott, P., Tarling, D., & Ward, M. (1961). Treatment of  
629 partially stable sedimentary rocks showing planar distribution of directions of  
630 magnetization. *Journal of Geophysical Research*, *66*(6).
- 631 Jackson, A., & Finlay, C. (2007). Geomagnetic secular variation and its applications  
632 to the core. In *Geomagnetism* (Vol. 5, p. 147-193). Elsevier.

- Jackson, A., Jonkers, A. R. T., & Walker, M. R. (2000). Four centuries of geomagnetic secular variation from historical records. *Phil Trans Roy Soc London, Series A*, 358(1768), 957-990.
- Johnson, C. L., Constable, C. G., Tauxe, L., Barendregt, R., Brown, L., Coe, R., ... Stone, D. (2008). Recent investigations of the 0-5 Ma geomagnetic field recorded in lava flows. *Geochemistry, Geophysics, Geosystems*, 9, Q04032. doi: doi:10.1029/2007GC001696
- Juarez, T., Tauxe, L., Gee, J. S., & Pick, T. (1998). The intensity of the earth's magnetic field over the past 160 million years. *Nature*, 394, 878-881.
- Kirschvink, J. L. (1980). The least-squares line and plane and the analysis of paleomagnetic data. *Geophys. Jour. Roy. Astron. Soc.*, 62, 699-718.
- Kissel, C., & Laj, C. (2004). Improvements in procedure and paleointensity selection criteria (PICRIT-03) for Thellier and Thellier determinations: Application to Hawaiian basaltic long cores. *Physics of the Earth and Planetary Interiors*, 147, 155-169.
- Koppers, A. (2003). High-resolution  $^{40}\text{Ar}/^{39}\text{Ar}$  dating of the oldest oceanic basement basalts in the western Pacific basin. *Geochem. Geophys. Geosys.*, 4, doi:10.1029/2003GC000574.
- Koppers, A., Russell, J., Jackson, M., Konter, J., Staudigel, H., & Hart, S. (2008). Samoa reinstated as a primary hotspot trail. *Geology*, 36, 435-438, doi:10.1130/G24630A.1.
- Koppers, A., Staudigel, H., & Wijbrans, J. (2000). Dating crystalline groundmass separates of altered Cretaceous seamount basalts by the  $^{40}\text{Ar}/^{39}\text{Ar}$  incremental heating technique. *Chem. Geol.*, 166, 139-158.
- Lawrence, K. P., Tauxe, L., Staudigel, H., Constable, C., Koppers, A., McIntosh, W. C., & Johnson, C. L. (2009). Paleomagnetic field properties near the southern hemisphere tangent cylinder. *Geochem. Geophys. Geosyst.*, 10, Q01005, doi:10.1029/2008GC00207.
- Leonhardt, R., Heunemann, C., & Krasa, D. (2004). Analyzing absolute paleointensity determinations: Acceptance criteria and the software thelliertool4.0. *Geochemistry, Geophysics, Geosystems*, 5.
- Livermore, P., Fournier, A., & Gallet, Y. (2014). Core-flow constraints on extreme archeomagnetic intensity changes. *Earth and Planet. Sci. Lett.*, 387, 145-156. doi: 10.1016/j.epsl.2013.11.020
- Lowes, F. (1973). Spatial power spectrum of the main geomagnetic field, and extrapolation to the core. *Geophysical Journal of the Royal Astronomical Society*, 36, 717-730.
- Mankinen, E., & Cox, A. (1988). Paleomagnetic investigation of some volcanic rocks from the McMurdo Volcanic Province, Antarctica. *Journal of Geophysical Research*, 93(B10), 11599-11612.
- McElhinny, M. (1973). *Paleomagnetism and plate tectonics*. Cambridge: Cambridge University Press.
- McElhinny, M. (2007). Encyclopedia of Geomagnetism and Paleomagnetism. In D. Gubbins & E. Herrero-Bervera (Eds.), (chap. Geocentric Axial Dipole Hypothesis). Springer-Verlag. doi: [https://doi.org/10.1007/978-1-4020-4423-6\\_107](https://doi.org/10.1007/978-1-4020-4423-6_107)
- McElhinny, M., & Lock, J. (1996). IAGA paleomagnetic databases with access. *Surveys in Geophysics*, 17(5), 575-591.
- McFadden, P. L., & McElhinny, M. (1982). Variations in the geomagnetic dipole 2: statistical analysis of VDMs for the past 5 m.y. *J. Geomag. Geoelectr.*, 34, 163-189.
- McFadden, P. L., Merrill, R. T., & McElhinny, M. W. (1988). Dipole/quadrupole family modeling of paleosecular variation. *J. Geophys. Res.*, 93, 11583-11588.
- Nagata, T., Arai, Y., & Momose, K. (1963). Secular variation of the geomagnetic total force during the last 5000 years. *J. Geophys. Res.*, 68, 5277-5282.

- Néel, L. (1955). Some theoretical aspects of rock-magnetism. *Adv. Phys.*, *4*, 191-243.
- Opdyke, N., & Henry, K. (1969). A test of the dipole hypothesis. *Earth and Planetary Science Letters*, *6*, 139-151.
- Paterson, G. (2011). A simple test for the presence of multidomain behavior during paleointensity experiments. *Journal of Geophysical Research*, *116*, B10104.
- Paterson, G., Tauxe, L., Biggin, A., Shaar, R., & Jonestrask, L. (2014). On improving the selection of Thellier-type paleointensity data. *Geochemistry Geophysics Geosystems*, *15*(4). doi: 10.1002/2013GC005135
- Pike, C., Roberts, A., & Verosub, K. (1999). Characterizing interactions in fine magnetic particle systems using first order reversal curves. *J. Appl. Phys.*, *85*, 6660-6667.
- Pike, C., Roberts, A., & Verosub, K. (2001). First-order reversal curve diagrams and thermal relaxation effects in magnetic particles. *Geophysical Journal International*, *145*, 721-730.
- Roberts, C., A.P. and Pike, & Verosub, K. (2000). First-order reversal curve diagrams: A new tool for characterizing the magnetic properties of natural samples. *Journal of Geophysical Research*, *106*, 28461-28475.
- Santos, C., & Tauxe, L. (2019). Investigating the accuracy, precision, and cooling rate dependence of laboratory-acquired thermal remanences during paleointensity experiments. *Geochemistry, Geophysics, and Geosystems*, *20*, 383-397.
- Selkin, P., Gee, J., & Tauxe, L. (2007). Nonlinear thermoremanence acquisition and implications for paleointensity data. *Earth and Planetary Science Letters*, *256*, 81-89.
- Selkin, P., & Tauxe, L. (2000). Long-term variations in paleointensity. *Phil. Trans. Roy. Soc. Lond.*, *358*, 1065-1088.
- Shaar, R., & Tauxe, L. (2013). Thellier\_gui: An integrated tool for analyzing paleointensity data from thellier-type experiments. *Geochem. Geophys. Geosys.*, *14*, 677-692.
- Shashkanov, V., & Metallova, V. (1972). Violation of Thellier's law for partial thermoremanent magnetizations. *Izv. Earth Physics*, *3*, 80-86.
- Shaw, J. (1974). A new method of determining the magnitude of the paleomagnetic field application to 5 historic lavas and five archeological samples. *Geophys. J. R. Astron. Soc.*, *39*, 133-141.
- Shcherbakov, V., McClelland, E., & Shcherbakova, V. (1993). A model of multidomain thermoremanent magnetization incorporating temperature-variable domain structure. *J. Geophys. Res.*, *98*(B4), 6201-6214.
- Smirnov, A. V., & Tarduno, J. A. (2003). Magnetic hysteresis monitoring of Cretaceous submarine basaltic glass during Thellier paleointensity experiments: evidence for alteration and attendant low field bias. *Earth Planet. Sci. Lett.*, *206*(3-4), 571-585.
- Stephenson, A. (1967). *Apparatus for the thermal demagnetization by the progressive method*. Chapman and Hall.
- Tanaka, H., & Kobayashi, T. (2003). Paleomagnetism of the late Quaternary Ontake Volcano, Japan: directions, intensities, and excursions. *Earth Planets and Space*, *55*(4), 189-202.
- Tanaka, H., Kono, M., & Uchimura, H. (1995). Some global features of paleointensity in geological time. *Geophys. J. Int.*, *120*, 97-102.
- Tauxe, L., Gans, P., & Mankinen, E. (2004). Paleomagnetism and  $^{40}\text{Ar}/^{39}\text{Ar}$  ages from volcanics extruded during the Matuyama and Brunhes Chrons near McMurdo Sound, Antarctica. *Geochemistry Geophysics Geosystems*, *5*(6).
- Tauxe, L., Gee, J., Steiner, M., & Staudigel, H. (2013). Paleointensity results from the Jurassic: New constraints from submarine basaltic glasses of ODP Site 801C. *Geochemistry Geophysics Geosystems*, *14*(10). doi: 10.1002/ggge/20282

- Tauxe, L., & Kent, D. V. (2004). A simplified statistical model for the geomagnetic field and the detection of shallow bias in paleomagnetic inclinations: Was the ancient magnetic field dipolar? In e. a. Channell J.E.T. (Ed.), *Timescales of the paleomagnetic field* (Vol. 145, p. 101-116). Washington, D.C.: American Geophysical Union.
- Tauxe, L., N., K., & Constable, C. (1991). Bootstrap statistics for paleomagnetic data. *Journal of Geophysical Research*, 96, 11723-11740.
- Tauxe, L., Shaar, R., Jonestrask, L., Swanson-Hysell, N., Minnett, R., Kopfers, A. A. P., ... Fairchild, L. (2016). PmagPy: Software package for paleomagnetic data analysis and a bridge to the Magnetics Information Consortium MagIC) database. *Geochem. Geophys. Geosyst.*, 17. doi: 10.1002/2016GC006307
- Tauxe, L., & Staudigel, H. (2004). Strength of the geomagnetic field in the Cretaceous Normal Superchron: New data from submarine basaltic glass of the Troodos Ophiolite. *Geochem. Geophys. Geosyst.*, 5(2), Q02H06, doi:10.1029/2003GC000635.
- Tauxe, L., & Yamazaki, T. (2015). Paleointensities. In M. Kono (Ed.), *Geomagnetism* (2nd Edition ed., Vol. 5, p. 461-509). Elsevier.
- Thébault, E., Finlay, C., Beggan, C., Alken, P., Aubert, J., Barrois, O., ... Lowes, F. (2015). International Geomagnetic Reference Field: the 12th generation. *Earth, Planets, and Space*, 67, 67-79. doi: 10.1186/s40623-015-0228-9
- Thellier, E. (1938). Sur l'aimantation des terres cuites et ses applications géophysique. *Ann. Inst. Phys. Globe Univ. Paris*, 16, 157-302.
- Thellier, E., & Thellier, O. (1959). Sur l'intensité du champ magnétique terrestre dans le passé historique et géologique. *Ann. Geophys.*, 15, 285-378.
- Vandamme, D. (1994). A new method to determine paleosecular variation. *Phys. Earth Planet. Int.*, 85, 131-142.
- Walton, D., & Shaw, J. (1922). Microwave demagnetization. *Journal of Applied Physics*, 71, 1549.
- Wang, H., Kent, D., & Rochette, P. (2015). Weaker axially dipolar time-averaged paleomagnetic field based on multidomain-corrected paleointensities from Galapagos lavas. *Proc. Nat. Acad. Sci.*, 112, 15036-15041. doi: 10.1073/pnas.1505450112
- Watkins, N. (1973). Brunhes epoch geomagnetic secular variation on Reunion Island. *Journal of Geophysical Research*, 78(32), 7763-7768.
- Yu, Y., Tauxe, L., & Genevey, A. (2004). Toward an optimal geomagnetic field intensity determination technique. *Geochemistry, Geophysics, Geosystems*, 5.
- Ziegler, L., Constable, C., Johnson, C. L., & Tauxe, L. (2011). PADM2M: a penalized maximum likelihood model of the 0-2 Ma palaeomagnetic axial dipole moment. *Geophys. J. Int.*.
- Zijderveld, J. D. A. (1967). *A.C. demagnetization of rocks: analysis of results*. Chapman and Hall.